Mehmet Sait DÜNDAR

Ph.D. Thesis

AGU 2024

TIME DISTRIBUTED CLASSIFICATION OF ALZHEIMER'S DISEASE ON MRI SCANS

Ph.D. THESIS
SUBMITTED TO THE DEPARTMENT OF ELECTRICAL AND COMPUTER ENGINGEERING
AND THE GRADUATE SCHOOL OF ENGINEERING AND SCIENCE
OF ABDULLAH GUL UNIVERSITY
IN PARTIAL FULFILLMENT OF THE REQUIREMENTS
FOR THE DEGREE OF
Ph.D.

By
Mehmet Sait DÜNDAR
June 2024

TIME DISTRIBUTED CLASSIFICATION OF ALZHEIMER'S DISEASE ON MRI SCANS

A THESIS
SUBMITTED TO THE DEPARTMENT OF ELECTRICAL AND COMPUTER ENGINGEERING
AND THE GRADUATE SCHOOL OF ENGINEERING AND SCIENCE OF ABDULLAH GUL UNIVERSITY
IN PARTIAL FULFILLMENT OF THE REQUIREMENTS
FOR THE DEGREE OF
Ph.D.

By
Mehmet Sait DÜNDAR
June 2024

SCIENTIFIC ETHICS COMPLIANCE

I hereby declare that all information in this document has been obtained in accordance with academic rules and ethical conduct. I also declare that, as required by these rules and conduct, I have fully cited and referenced all materials and results that are not original to this work.

Name-Surname: Mehmet Sait DÜNDAR

Signature:

REGULATORY COMPLIANCE

Ph.D. thesis titled “Time Distributed Classification of Alzheimer’s Disease on MRI Scans” has been prepared in accordance with the Thesis Writing Guidelines of the Abdullah Gül University, Graduate School of Engineering & Science.

Prepared By	Advisor
Mehmet Sait DÜNDAR	Prof. Bülent YILMAZ

Head of the Electrical and Computer Program

Asst. Prof. Samet GÜLER

ACCEPTANCE AND APPROVAL

Ph.D. thesis titled Time Distributed Classification of Alzheimer's Disease on MRI Scans and prepared by Mehmet Sait DÜNDAR has been accepted by the jury in the Electrical and Computer Engingeering Graduate Program at Abdullah Gül University, Graduate School of Engineering & Science.

26/06/2024

JURY:

Advisor: Prof. Bülent YILMAZ

Member: Prof. Osman EROĞUL

Member: Prof. Mahmut TOKMAKÇI

Member: Assoc. Prof. Özkan Ufuk NALBANTOĞLU

Member: Asst. Prof. Hakan AKSEBZECİ

APPROVAL:

The acceptance of this Ph.D. thesis has been approved by the decision of the Abdullah Gül University, Graduate School of Engineering & Science, Executive Board dated ……/……/2024 and numbered …….

……/……/2024

Graduate School Dean

Prof. İrfan ALAN

ABSTRACT

TIME DISTRIBUTED CLASSIFICATION OF ALZHEIMER'S DISEASE ON MRI SCANS

Mehmet Sait DÜNDAR

Ph.D. in Electrical and Computer Engineering

Advisor: Prof. Bülent YILMAZ

June 2024

This thesis presents a comprehensive framework for studying Alzheimer's Disease (AD) progression by focusing on the classification of AD, Mild Cognitive Impairment (MCI), and Cognitively Normal (CN) individuals using advanced machine learning models that analyze changes in brain volumetrics over time through MRI scans. In the first phase of the research, MR images from the Alzheimer's Disease Neuroimaging Initiative database were utilized, which included sequences of 3-4 scans taken annually from 22 CN, 18 AD, and 20 MCI subjects. Key volumetric parameters such as cortical thickness and intracranial volumes were extracted using the CAT12 toolbox in SPM software. A novel classification method based on the rate of volumetric changes over time was employed, effectively capturing the progressive nature of neurological changes. This approach achieved accuracies of 82.5% in distinguishing AD from CN, 71% in differentiating MCI from AD, and 69% in separating MCI from CN, alongside a 55% accuracy in a three-way classification using random forest and support vector machines.

Building on these initial insights, the second phase of the study significantly advanced the methodology by integrating a pre-trained 3D ResNet-101 CNN algorithm for initial spatial categorization of MRI scans, followed by the use of Long Short-Term Memory (LSTM) networks. These LSTMs processed the same sequences of 3-4 annual scans for each patient, enhancing the model's ability to analyze and interpret the temporal progression of volumetric changes. This sophisticated approach led to marked improvements in classification accuracy: 96.7% in differentiating AD from CN, 87.5% in distinguishing AD from MCI, and 86.4% in separating MCI from CN. The study effectively demonstrates a significant enhancement in capturing the temporal dynamics of AD progression.

Keywords: Alzheimer's Disease, MRI, Temporal Analysis, 3D CNN, LSTM

ÖZET

MRG TARAMALARINDA ALZHEIMER HASTALIĞININ ZAMAN DAĞILIMLI SINIFLANDIRILMASI

Mehmet Sait DÜNDAR

Elektrik ve Bilgisayar Mühendisliği Anabilim Dalı Doktora

Tez Danışmanı: Prof. Dr. Bülent YILMAZ

Haziran 2024

Bu tez, Alzheimer Hastalığı (AD) ilerlemesini incelemek için gelişmiş makine öğrenimi modelleri kullanarak AD, Hafif Bilişsel Bozukluk (MCI) ve Bilişsel Olarak Normal (CN) bireyleri zaman içinde beyin hacimsel verilerinin değişimini analiz ederek sınıflandırmaya odaklanmaktadır. Araştırmanın ilk aşamasında, Alzheimer Hastalığı Nörogörüntüleme Girişimi veri tabanından alınan MR görüntüleri kullanılmıştır; bu görüntüler 22 CN, 18 AD ve 20 MCI bireyden oluşan yıllık 3-4 tarama dizisini içermektedir. CAT12 araç kutusu kullanılarak SPM yazılımında kortikal kalınlık ve intrakraniyal hacimler gibi temel hacimsel parametreler çıkarılmıştır. Zaman içinde hacimsel değişikliklerin oranına dayanan yeni bir sınıflandırma yöntemi uygulanmış; bu yöntem AD'yi CN bireylerden ayırt etmede %82,5, MCI'yi AD'den ayırt etmede %71 ve MCI'yi CN bireylerden ayırt etmede %69 doğruluk sağlamıştır; üç yönlü sınıflandırmada ise %55 doğruluk elde edilmiştir.

Araştırmanın ikinci aşamasında, metodoloji önemli ölçüde geliştirilerek, MRI taramalarının ilk kategorizasyonu için önceden eğitilmiş 3D ResNet-101 CNN algoritması entegre edilmiştir ve ardından her hastanın yıllık 3-4 tarama dizisini işlemek üzere Uzun Kısa Süreli Hafıza (LSTM) ağları kullanılmıştır. Bu gelişmiş yaklaşım, hacimsel değişikliklerin zaman içindeki ilerlemesinin analizini ve yorumlanmasını önemli ölçüde geliştirerek sınıflandırma doğruluğunda belirgin iyileşmeler sağlamıştır: AD ile CN bireyler arasında %96,7, AD ile MCI arasında %87,5 ve MCI ile CN bireyler arasında %86,4 doğruluk elde edilmiştir. Araştırma, AD ilerlemesinin zaman dinamiklerini yakalama konusunda önemli bir gelişme göstermiştir.

Anahtar Kelimeler: Alzheimer Hastalığı, MRG, Zamansal Analiz, 3D CNN, LSTM

ACKNOWLEDGEMENTS

I would like to express my deepest gratitude to Prof. Bülent YILMAZ, my advisor at Abdullah Gül University, for his invaluable guidance and mentorship throughout my doctoral studies. His insights and expertise have been a cornerstone of my academic journey, and for that, I am profoundly indebted.

My heartfelt thanks also go to my father Munis DÜNDAR and my mother Gökçen DÜNDAR and my sisters, whose unwavering support and encouragement have been a constant source of motivation during my research endeavors. Their belief in me has been a guiding light, inspiring me to persevere through the challenges of academic research.

My sincere appreciation extends to my loving wife, Gülhan DÜNDAR, whose love, patience, and unwavering support have been my constant source of strength and inspiration. Her encouragement and understanding have been crucial in navigating the challenges of my academic life.

I am also grateful to Assoc. Prof. Gökmen ZARARSIZ for his assistance with the statistical analysis of this article. His expertise and contributions were instrumental in enriching the quality and accuracy of the research.

Furthermore, I am grateful for the financial support provided by the Council of Higher Education in Turkey (YÖK), under the grant YOK 100/2000, during my doctoral studies.

Data collection and sharing for this thesis was funded by the Alzheimer's Disease Neuroimaging Initiative (ADNI) (National Institutes of Health Grant U01 AG024904) and DOD ADNI (Department of Defense award number W81XWH-12-2-0012).

TABLE OF CONTENTS

LIST OF FIGURES

LIST OF TABLES

LIST OF ABBREVIATIONS

AD	Alzheimer's Disease
MCI	Mild Cognitive Impairment
CN	Cognitively Normal
LSTM	Long Short-Term Memory
PET	Positron Emission Tomography
MR	Magnetic Resonance
fMRI	functional Magnetic Resonance Imaging
DTI	Diffusion Tensor Imaging
PET	Positron Emission Tomography
RF	Radio frequency
NMV	Net Magnetization Vector
FID	Free Induction Decay
LSTM	Long Short-Term Memory
TR	Repetition Time
TE	Echo Time
FOV	Field of View
FFT	Fast Fourier Transform
SNR	Signal-to-Noise Ratio
NSA	Number of Signal Averages
NEX	Number of Excitations
NPE	Number of Phase Encoding Steps
ML	Machine Learning
PCA	Principal Component Analysis
DQN	Deep Q Networks
SVM	Support Vector Machines
k-NN	K-Nearest Neighbors
CNNs	Convolutional Neural Networks
RNNs	Recurrent Neural Networks
ReLUs	Rectified Linear Units
PD	Parkinson's disease
SPM	Statistical Parameter Mapping

CSF	Cerebrospinal Fluid
TIV	Total Intracranial Volume
CT	Cortical Thickness
WM	White Matter
GM	Grey Matter
HSD	Tukey's Honestly Significant Difference
NLP	Natural Language Processing
VQA	Video Quality Assessment
VQM	Video Quality Metric
SGD	Stochastic Gradient Descent

To my supporting family.

CHAPTER 1

INTRODUCTION

Alzheimer's Disease (AD), as the most prevalent form of dementia, accounts for an estimated 60-80% of cases, underscoring its significance in public health. This neurodegenerative disorder predominantly affects older adults, with around 11% of individuals aged 65 and above suffering from AD, as per the Alzheimer's Association [1]. This prevalence increases with age, making AD a major concern in aging societies worldwide [2]. The disease not only impacts the cognitive functions of the patients but also places a significant burden on caregivers, healthcare systems, and society at large [3].

AD is characterized by the accumulation of amyloid-beta plaques and tau protein tangles in the brain, leading to neuronal damage and loss [4]. This pathology is associated with a progressive decline in cognitive functions, most notably memory [1]. The disease typically progresses through several stages, starting from preclinical Alzheimer's, where changes in the brain occur without noticeable symptoms, to mild cognitive impairment (MCI), and eventually to full-blown Alzheimer's dementia.

MCI is a critical stage in the continuum of AD. It represents a transitional phase where the cognitive decline is more severe than expected for an individual's age and education level but does not yet interfere significantly with daily activities [5]. Not every individual with MCI develops AD; however, they are at a higher risk compared to those without MCI. Research suggests that between 10 and 15% of individuals with MCI progress to AD annually [6].

The global burden of AD is substantial and growing. Projections estimate that about 1.2% of the world's population will suffer from AD by 2046 [7]. This increase is primarily due to the aging population, as the risk of AD increases significantly with age [8]. Such

statistics highlight the need for effective strategies for early detection, intervention, and care.

Diagnosing AD remains a challenge, particularly in its early stages. Currently, clinical evaluation, including medical history, neurological exams, and cognitive tests, is the gold standard for diagnosing AD [9]. However, these methods often come into play when noticeable symptoms have already developed, making early intervention difficult.

Recent advancements have emphasized the potential of MRI in detecting AD in its nascent stages. MRI can visualize brain structure and detect changes even before symptoms appear [10]. Researchers are exploring the use of advanced MRI techniques to identify specific biomarkers associated with early AD, such as brain atrophy patterns, changes in white matter integrity, and reduced cerebral blood flow.

Apart from traditional MRI, other neuroimaging modalities like functional MRI (fMRI), Diffusion Tensor Imaging (DTI), and Positron Emission Tomography (PET) are being investigated for their potential in early AD diagnosis [11]. These techniques provide insights into the functional and metabolic changes in the brain, offering a more comprehensive understanding of the disease's progression.

Early detection of AD through advanced imaging techniques could revolutionize the approach to treatment and care. Identifying AD at a pre-symptomatic stage may enable interventions that could delay the onset of symptoms, alter the disease trajectory, or potentially prevent the progression to full-blown dementia [12]. This early intervention approach could significantly reduce the burden on patients, caregivers, and healthcare systems.

Research in Alzheimer's disease is rapidly evolving, with a focus on developing more sensitive diagnostic tools, understanding the molecular mechanisms underlying the disease, and discovering new therapeutic targets [13]. The integration of neuroimaging with other biomarkers, such as genetic and molecular markers, could lead to a more personalized approach to AD diagnosis and treatment [14].

In conclusion, Alzheimer's Disease remains a significant challenge in the realm of neurodegenerative disorders. The progression from MCI to AD, the increasing global prevalence, and the urgent need for early detection underscore the importance of advancements in diagnostic techniques like MRI. The future of AD research and

management lies in the early detection and intervention, which holds the promise of altering the course of this debilitating disease and improving the quality of life for millions of affected individuals and their families.

CHAPTER 2

BACKGROUND

2.1. Magnetic Resonance Imaging

Magnetic Resonance Imaging (MRI) is one of the most widely used biomedical imaging methods today. Images are created digitally using magnetism and radio waves through mathematical transformations and computer programming.

In MRI, living tissue is stimulated with RF (radio frequency) waves. The MRI signal is obtained from atomic nuclei, primarily hydrogen atoms, which consist of a single proton and make up a large part of the human body. This is why hydrogen is typically the atom stimulated and from which signals are received in MRI.

For MRI imaging, the human body must first be placed in a magnetic field significantly stronger than the earth's magnetic field. This field enables hydrogen protons in the body to be stimulated.

Once stimulated, the atomic nuclei absorb the RF energy, altering their energy levels. When the RF is discontinued, they return to their original energy levels, releasing the energy they absorbed. This emitted energy is read and digitized by a computer, and these data are processed to create an MRI image.

One of the limitations of MRI is the long duration of imaging and the complexity of selecting image parameters. However, MRI has several important advantages over other radiological imaging devices.

The most significant advantage is that MRI does not use ionizing radiation, which has the potential to ionize atoms. This means it can cause significant damage to cells or tissues in the human body and lead to DNA mutations [15].

Another advantage of MRI is its ability to provide high-resolution images of soft tissues, unlike other radiological imaging devices. Moreover, bone tissue does not hinder imaging, allowing images to be obtained from every region or section.

Additionally, the image acquisition methods, mathematical processes, and programs used in MRI allow the modification of imaging parameters, sequences, and techniques. This adaptability makes MRI a continually evolving radiological imaging method.

MRI's image formation process involves complex physical and mathematical operations, making it one of the most engineering-intensive among biomedical devices. Images in MRI are created utilizing magnetism and resonance.

Magnetism is a physical phenomenon arising from the repulsive or attractive forces between materials, measured in Tesla [16]. The magnetic field is the area of influence of a magnet, with the force exerted within this field known as the magnetic force.

The magnetic field is generated by the movement of electric current and is measured in Gauss. Earth's magnetic field is approximately 0.5 Gauss. One Tesla is equivalent to 10,000 Gauss. The direction of a magnetic field can be clockwise or counterclockwise relative to the direction of the electric current.

The right-hand rule helps determine the direction of the magnetic field: if the right thumb points in the direction of the current, the fingers show the direction of the magnetic field.

Electric current changes also generate a magnetic field, and conversely, changes in a magnetic field can induce electric current. The current generated in a closed system by moving a magnet is called induced current.

An atom consists of protons, neutrons, and electrons. Protons and neutrons are in the nucleus, while electrons orbit around the nucleus. Protons are positively charged, electrons are negatively charged, and neutrons are neutral. The atomic number equals the number of protons, and the mass number equals the total number of protons and neutrons, as electrons have negligible mass.

Protons and neutrons spin around their own axis in the nucleus, a motion known as spin [17]. The direction of these spins is random. Atoms with an even number of protons and neutrons in their nucleus have spins that neutralize each other, resulting in a net spin of zero. Atoms with an odd number of protons and/or neutrons have a net spin.

Moving protons, due to their spin, possess a magnetic moment (magnetic moment = gamma × angular momentum of spin), creating a magnetic field. Atoms with an odd number of protons and/or neutrons, like the hydrogen atom, which contains only one proton, are referred to as MRI-active atoms [17]. Hydrogen atoms are particularly important in MRI due to their abundance in the human body in water and fat and their large magnetic moment, facilitating better measurement of their magnetic field.

Under normal conditions, the magnetic moments of MRI-active atoms are randomly oriented, preventing them from collectively forming a magnetic field. However, when placed within a magnetic field, they align with the field's direction, creating a net magnetization, which is crucial for image formation in MRI.

In MRI, this magnetization is examined using an external magnetic field denoted as B0. Within this field, MRI-active atoms align either parallel or antiparallel to the field. There are slightly more atoms aligned parallel than antiparallel in a magnetic field of 1.5 Tesla, the difference in numbers being about 4 in 1 million. Despite this small difference, the vast number of hydrogen atoms in human tissue provides sufficient data for MRI imaging [18].

When placed in a magnetic field, atoms exhibit precession, a movement where the tip of the magnetic vector traces a circular path around the external magnetic field axis, similar to a spinning top.

The frequency of precession in a specific magnetic field is determined by the Larmor equation (2.1), crucial for MRI [19].

$$\omega_0 = \gamma . \beta_0 \tag{2.1}$$

In this equation, ω_0 represents the precession frequency, β_0 the magnetic field, and γ the gyromagnetic constant of the atom in a 1 Tesla magnetic field. According to this equation, the precession frequency of a hydrogen atom in a 1T field is 42.57MHz, and this frequency increases proportionally with the strength of the magnetic field.

Resonance occurs when energy is transferred to a system oscillating at a particular frequency, matching that frequency. In MRI, resonance occurs when RF pulses, at the same frequency as the hydrogen atom and perpendicular to the B_0 magnetic field, are applied. Each atom has a different gyromagnetic constant; thus, these pulses only resonate with the hydrogen atom, not affecting other MRI-active atoms.

During resonance, two phenomena occur: energy absorption and phase coherence. Energy absorption refers to the energy absorbed and emitted by hydrogen atoms from the RF pulses. This absorption occurs in the B_0 magnetic plane with the RF pulses, increasing the energy of the hydrogen atom and affecting its spin motion.

The Net Magnetization Vector (NMV) is the sum of the magnetic moments of the hydrogen atoms. If the spinning hydrogen atoms have equal numbers of parallel and antiparallel spins, the NMV is zero. NMV can be discussed as a magnetic vector between the transverse and vertical planes, perpendicular to each other. The angle between NMV and the vertical plane is called the "flip angle."

Furthermore, resonating hydrogen atoms align their magnetic moments in the same phase, known as phase coherence. When hydrogen atoms' spins are in the same phase, NMV oscillates in the transverse plane at the Larmor frequency.

According to Faraday's law, a change in magnetic flux through a loop induces voltage. Thus, the rotation of NMV in the transverse magnetization plane during resonance induces voltage in MRI coils, generating the MR signal.

When the RF pulse is discontinued, the signal to the coils decreases because the NMV's transverse magnetization diminishes, leading to a reduction in the voltage generated in the coils. This phenomenon is known as Free Induction Decay (FID).

After the application of the RF pulse, the spins attempt to return to their initial state. This is because the NMV (Net Magnetization Vector), which has moved to the transverse magnetization plane due to the RF pulse, tries to return to the longitudinal magnetization plane when the RF is stopped. In this process, longitudinal magnetization increases, while transverse magnetization decreases.

The increase in longitudinal magnetization is called T1 relaxation, while the decrease in transverse magnetization is called T2 relaxation. Although T1 and T2 times may seem similar, the loss of transverse magnetization, affected by spin-spin interactions and microscopic magnetic field inhomogeneity, makes T2 relaxation faster. Therefore, the T1 value is always greater than T2.

T1 relaxation is the increase in longitudinal magnetization of the NMV after the RF pulse is stopped [20].

T1 time refers to the duration it takes for the NMV to acquire 63% of its longitudinal magnetization in the longitudinal magnetic plane. Each tissue has a different T1 time. Water's T1 time is longer than that of fat. The T1 time is longer in higher Tesla environments.

T2 relaxation is the loss of transverse magnetization that occurs after the RF pulse is stopped [20]. T2 relaxation, due to losses in transverse magnetization caused by spin-spin interactions and microscopic magnetic field inhomogeneity, differs from the T1 relaxation time.

T2 time is the duration it takes for the NMV to lose 63% of its transverse magnetization.

Like T1, each tissue has a different T2 time, and water's T2 time is longer than that of fat. T2 time is independent of the magnetic environment, meaning water's T2 time is the same at 1.5T and 3T.

An MRI image consists of black and white pixels. This is because high signals come from the white parts inside the MRI machine, and low signals come from the black parts. The signal differences resulting from tissue variations make the image distinguishable.

If a tissue appears white in an MRI image, it means the tissue has high transverse magnetization; hence, the MRI coil receives a high magnetization power, resulting in a high signal. The opposite is true for tissues appearing black, where transverse magnetization is low, the MRI coil's received magnetization power is less, and consequently, the overall signal is lower.

The controllable contrast parameters of an MRI machine include TR (Repetition Time), TE (Echo Time), and flip angle. TR is the time between two RF pulses, while TE is the time between the RF pulse and signal measurement. The uncontrollable parameters of the machine are T1, T2, and proton density.

In T1-weighted MRI images, tissues with high T1 times appear dark, while in T2-weighted images, tissues with high T2 times appear bright.

A long TR period negates the T1 effect; a short TE period negates the T2 effect. Therefore, for T1-weighted imaging, a short TR and short TE period should be used. In T1-weighted imaging, water appears dark, and fat appears bright. This imaging technique is mostly used for anatomical imaging.

For T2-weighted imaging, a long TR and long TE period should be used. In T2-weighted imaging, water appears bright, and fat appears dark. This imaging technique is primarily used for pathological imaging.

Proton density-weighted imaging, as the name suggests, provides images based on proton density. Tissues with high proton density appear bright, while those with low proton density appear dark. For proton imaging, a long TR and short TE period should be used.

MRI images are produced using pulse sequences. A pulse sequence includes both RF and gradient pulses [17]. Pulse sequences are used to direct the spins. Without pulse sequences, the necessary signal for creating the desired image would not be obtained due to phase dispersion immediately after the RF pulse is stopped. Additionally, it would be impossible to determine the origin of the signal.

The B_0 magnetic field in the MRI device is always on. RF and gradients are activated and sent to obtain the desired image. Slice selection, phase encoding, and frequency encoding axes are perpendicular to each other.

Spins also lose phase coherence due to spin-spin interaction and magnetic field inhomogeneity. No matter how much effort is made to correct magnetic field inhomogeneity, it cannot be made perfect, and thus, microscopic level inhomogeneity inevitably occurs in the magnetic field.

According to the Larmor equation, spins affected by inhomogeneity have changes in frequency and phase, leading to exponential signal loss. This is referred to as FID (Free Induction Decay), and the lost value is termed T2*.

The main purpose of the pulse sequence is to determine the origin of the signal by making changes in magnetic gradients and to obtain the desired image by altering TE and TR. The RF pulse brings the spins to the same phase. Additionally, spins can be rephased using a 180-degree RF pulse.

In MRI, image acquisition is based on the different relaxation times of various tissues. In this process, the movement of the NMV in the transverse plane due to resonance causes voltage in MRI coils. This voltage comprises the signals necessary for image formation in MRI. Coils collect the entire signal from the volume. Gradients help determine the exact point of the signal's origin within a specific volume [21].

Gradients in an MRI device are created using gradient coils. The current in the coils is altered to manipulate the strength of the magnetic field, allowing control over the resulting signal. This control is achieved by creating a linear difference in the magnetic field.

Despite the linear change in the magnetic field, the strength of the magnetic field in the center remains unchanged and increases linearly with distance from the center. The magnitude of the gradient increases the slope of the linear change, causing a more significant change in the magnetic field at a given distance. Conversely, decreasing the gradient power has the opposite effect.

The polarity of the gradient determines whether the force affecting the B_0 magnetic field is positive or negative, depending on the direction of the current. Also, increasing the magnitude of the gradient enhances the received signal and, consequently, the resolution.

The rate of change in the gradient's magnitude, i.e., the ratio of the maximum gradient magnitude to the rise time, is known as the slew rate. The slew rate determines the measurement speed in an MRI device. Each MRI device has a maximum slew rate it can manage.

The precession frequencies of hydrogen atoms' magnetic moments are proportional to the strength of the magnetic field. Thus, the frequency of the signal received from a patient in the MRI, altered by the gradient, varies depending on the signal's location. Additionally, the phase of precession is also affected by the strength of the magnetic field.

With the linear change induced by the gradient, the precession frequency and phase also change linearly. This allows the location of the MRI signal to be determined in three dimensions. However, for this to be possible, all gradients must be perpendicular to each other. The gradients responsible for three-dimensional signal acquisition are named as follows: Slice selection, frequency encoding, phase encoding.

The slice selection gradient, as the name suggests, is used to select the slice of the MRI image.

When the gradient linearly changes the magnetic field strength, the hydrogen atoms' magnetic moments in a slice will all have the same precession frequency. Thus, only the selected slice can be stimulated with RF pulses of the same frequency, ensuring data is obtained only from that slice.

In an MRI machine, the Z gradient is generally used for vertical slice selection, the Y gradient for phase encoding, and the X gradient for frequency encoding. The slice-selective gradient is sent simultaneously with the RF pulses.

After applying the slice selection gradient, a 180-degree gradient is applied to bring the hydrogen atoms to the same phase. This is called the rephase gradient [22].

Each RF frequency has a bandwidth that affects the thickness of the slice. Increasing the bandwidth increases the slice thickness.

After slice selection, the hydrogen atoms in that slice have the same magnetic field strength as the system. The frequency of the spins in the slice and the frequency of the signal from the slice will be equal to the frequency in the Larmor equation. From this point, two-dimensional positional information is needed to determine from which point in the slice the data comes.

The frequency shift that occurs along the frequency encoding gradient results in a frequency shift. This means that hydrogen atoms exposed to a higher magnetic field strength will have a higher frequency. This is known as frequency encoding.

The frequency encoding gradient is kept on during signal acquisition. Therefore, the frequency encoding gradient is also called the signal readout gradient.

The change curve in frequency encoding determines the size of the FOV (Field of View) and, consequently, the resolution of the image. The greater the change in frequency encoding, the larger the FOV.

The gradient changes the magnetic strengths of the hydrogen atoms in a slice and also their phases.

During the application of the phase encoding gradient, the precession frequency changes depending on the position. When the phase encoding gradient is turned off, the frequency differences in different positions become equalized, but there is now a phase difference in the signals coming from different locations. This phase difference is used for signal localization. The resulting phase difference depends on the magnitude and duration of the phase encoding gradient.

K-space is where the digitized raw data is stored [17]. It is a virtual space where signals related to the image are collected, stored, and processed. K-space is not an image, but a

spatial domain that contains information about the frequency and location of the signal coming from the MRI.

K-space is a two-dimensional rectangle. The k_x axis of K-space is the frequency axis, and the k_y axis is the phase axis.

The center of K-space contains signal and contrast information of the MRI image, while its periphery forms the resolution of the image. Thus, the most important data in K-space are concentrated in its center.

Less phase encoding data is present in the center of K-space, and phase shift is minimal. The MRI signal is strongest at the center, but the spatial signal necessary for resolution is minimal. Conversely, more phase encoding data and significant phase shift are present farther from the center of K-space. The MRI signal is weaker here, but the spatial signal is greater.

K-space is initially filled with the central lines, followed by outward expansion through phase shift creation. For example, if the center of K-space is considered as k_x, the line above the k_x axis is filled first, followed by the line below the k_x axis, then two lines above, and so on.

Each data entry in K-space is sorted based on signal strength, phase, and frequency. This sorting is done through FFT (Fast Fourier Transform) [23]. The FFT of the obtained signal in MRI is taken, and after the signal is transferred to the frequency domain, it is written to K-space.

Through spatial encoding, phase shifts in spins result in data from different frequencies filling each line, clearly identifying the point of origin for the data.

To obtain data from all points, all three gradients are used. Therefore, the system needs a certain amount of time to open and close the gradients. This duration depends on the power of the gradients, their opening and closing mechanisms, and their design. However, regardless of how the pulse mechanism is designed, echo acquisition cannot be performed without applying all gradients. Thus, the minimum TE time depends on the gradients.

There are different types of K-space acquisition. The most commonly used is Cartesian sampling. However, non-Cartesian sampling techniques such as spiral acquisition and radial acquisition can also be used to obtain K-space.

In addition to 2D acquisition techniques, images can be obtained using 3D acquisition techniques in 3D K-space. In this technique, the RF pulse stimulates the entire brain, and the signal is obtained from the volume instead of the slice [24].

Once signals are converted into data filling K-space, the process of transforming this data into an image begins. This image creation process involves the inverse Fourier transform of the data in K-space.

Every image contains an FOV value, determining the size (cross-sectional area) of the anatomical image. The number of pixels in the FOV is equal to the number of samples in phase and frequency encoding. The sampling interval in K-space is equal to 1/FOV. For instance, if K-space consists of a 128x128 matrix and FOVX and FOVY are 220mm, then the sampling interval $\Delta kx = \frac{1}{FOV} = \frac{1}{220} mm.$

FFT (Fast Fourier Transform) is a process where data is transformed from the time domain to the frequency domain. This allows for each signal to be sorted by frequency, enabling frequency encoding in k-space, and determining the spatial location of each pixel.

In MRI, a one-dimensional signal undergoes Fourier transformation when written to k-space, as shown in equation 2.2.

$$S(k) = \int_{-\infty}^{\infty} I(x) e^{-i2\pi kx} dx \tag{2.2}$$

In this equation, S(k) represents the k-space, and I(x) represents the image. The data in k-space is converted to an image by undergoing an inverse Fourier transformation, as shown in equation 2.3.

$$I(x) = \int_{-\infty}^{\infty} S(k) e^{i2\pi kx} dk \tag{2.3}$$

The dimensions of an image obtained through MRI depend on the sampling in the frequency encoding axis, phase encoding axis, and slice thickness. The frequency and phase encoding sampling numbers, NFE and NPE respectively, are determined by the operator. Here, the pixel number Pix is given by FOV/N.

Achieving an ideal image in MRI is contingent on various parameters, including the Signal-to-Noise Ratio (SNR) and the magnetic field strength of the MRI device.

SNR, or Signal-to-Noise Ratio, represents the ratio of the signal to noise. A higher SNR indicates lower noise in the obtained image. SNR depends on several factors, including MRI hardware (magnetic field of the MRI, RF coils), relaxation parameters, and chosen pulse sequence parameters. Low SNR can lead to image blur, reduced contrast change, loss of detail, and consequently diagnostic challenges.

Noise in SNR can originate from the device or the patient. Fluctuations in the current on the device's coils, conductive surface, or patient's electrical path can affect the magnetic field, leading to voltage variations and thus noise. Using smaller coils can help reduce noise.

CNR, or Contrast-to-Noise Ratio, is the ratio of contrast to noise. Contrast refers to the color difference and distinguishability between two different tissues in the image. The greater the signal difference between two tissues, the higher the contrast. Low CNR implies reduced contrast difference and difficulty in tissue distinguishability.

The smallest observable object in an MRI image is one pixel. The number of pixels in an image determines its resolution. The visibility of detail in an MRI image depends on adequate resolution, contrast difference between surrounding tissues, and high SNR.

A signal can be sampled multiple times with the same phase encoding. In such cases, the same line in k-space is filled multiple times. The number of these samplings is referred to as NSA (Number of Signal Averages) or NEX (Number of Excitations). As the NSA/NEX number increases, more data is written to each line in k-space, leading to increased data storage in k-space and longer imaging times.

For Cartesian acquisition: Imaging time = TR × NPE × Number of Slices × NSA.

In MRI imaging, several parameters influence voxel size, signal-to-noise ratio (SNR), and imaging time, each impacting image quality and scan efficiency. Increasing slice thickness generally leads to a larger voxel size and higher SNR, as a larger volume of spins contributes to the signal; however, the increase in SNR is more accurately proportional to the square root of the voxel volume rather than being strictly linear. Similarly, an increase in the Field of View in Phase Encoding Direction (FOVPE) raises both voxel size and SNR.

The Number of Phase Encoding Steps (NPE) has an inverse effect on voxel size, decreasing it, while SNR improves as the square root. Imaging time increases linearly

with NPE, balancing image detail with scan duration. The Number of Signal Averages/Number of Excitations (NSA/NEX) enhances SNR as the square root and extends imaging time linearly without affecting voxel size.

Adjustments in bandwidth typically decrease SNR due to a shorter frequency encoding time, impacting chemical shift and susceptibility artifacts. This decrease is not directly proportional to the bandwidth itself. Repetition Time (TR) influences SNR in a complex way: longer TR allows for more complete longitudinal magnetization recovery, increasing SNR, but not linearly. Echo Time (TE) increases lead to more transverse magnetization decay, reducing SNR. The specific effects of TR and TE adjustments depend on tissue properties and the MRI sequence type.

Lastly, the type and size of the coil significantly affect SNR. Smaller coils or those closer to the area of interest, like surface coils, can provide higher SNR for that specific region but may not be suitable for imaging larger or deeper structures. These interactions between MRI parameters highlight the importance of careful selection to meet specific diagnostic needs, optimizing image quality while managing efficient scan times.

A voxel represents the 3D counterpart of a pixel. Also, the sampling frequency should be twice the frequency of the sampled signal. Hence, the maximum frequency of the measured signal should be half the sampling frequency, known as the Nyquist limit (Equation 2.4).

$$f_{Nyquist} = \frac{f_{sampling}}{2} \tag{2.4}$$

If the signal frequency exceeds the Nyquist frequency ($f_{signal} > f_{Nyquist}$), the signal appears at a lower frequency, causing overlapping of measured signals, known as "aliasing." This phenomenon is referred to as aliasing artifact in MRI.

Artifacts in MRI are elements that appear in the image but do not originate from the object being imaged. They can arise from missing signals, excess signals, or mixed signals. Types of artifacts include motion artifacts, imaging technique-induced artifacts, metal and susceptibility artifacts, and hardware-based artifacts.

A quench in MRI occurs when the magnetic coils heat up beyond absolute zero, losing their superconductivity and gaining resistance. This results in the rapid vaporization of helium within the MRI. Quenches in MRI are rare but can occur spontaneously. However,

they are also performed deliberately when a metal object sticks to the MRI machine, causing it to lose magnetization. This procedure is costly and is therefore only undertaken in emergencies or when absolutely necessary.

2.2. Machine Learning

Machine Learning (ML) is a field of artificial intelligence focused on developing algorithms and models that enable computers to learn from and make decisions based on data. Its origins trace back to the mid-20th century, with early work by Alan Turing and Arthur Samuel. Samuel's checkers-playing program is often cited as one of the earliest instances of ML in action.

There are several types of machine learning, each with its own approach and algorithms. In supervised learning, models are trained on labeled datasets, meaning the data includes the desired output. For instance, linear regression, a fundamental algorithm in supervised learning, is used for predicting numeric values by modeling the relationship between a dependent variable and one or more independent variables [25]. Another supervised learning algorithm is logistic regression, typically used for classification tasks.

Unsupervised learning involves models that learn from unlabeled datasets (Figure 2.1). These algorithms, such as k-means clustering and hierarchical clustering, identify patterns and relationships in the data. Principal Component Analysis (PCA) is another unsupervised learning technique, widely used for dimensionality reduction while preserving the essential patterns in the dataset.

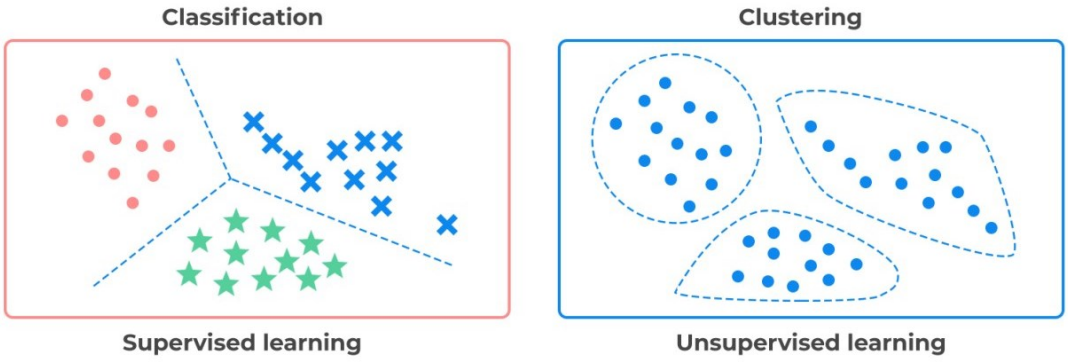

Figure 2.1 Supervised & Unsupervised learning [26]

Reinforcement learning is characterized by an agent that learns to make decisions by performing actions and receiving rewards or penalties. Algorithms such as Q-learning and Deep Q Networks (DQN) are prominent in this type of learning, especially in applications like game playing and real-time decisions [27].

Among the key algorithms in machine learning, Support Vector Machines (SVM) stand out. Effective in high-dimensional spaces, SVM is used for both classification and regression tasks. It works by finding a hyperplane in an N-dimensional space that distinctly classifies the data points (Figure 2.2).

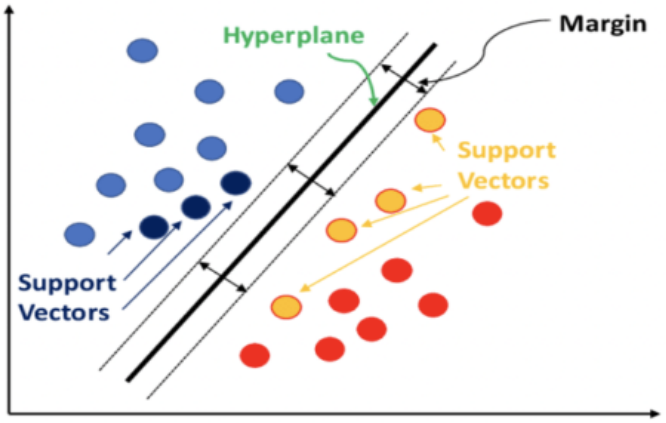

Figure 2.2 Support Vector Machines (SVM) [28]

Naïve Bayes classifiers are a family of simple probabilistic classifiers based on applying Bayes' theorem with strong (naïve) independence assumptions between the features (Figure 2.3). They are particularly effective for categorization tasks and are a popular choice for text classification problems where the data dimensionality is high, such as in spam filtering and sentiment analysis applications. Despite their simplicity, Naïve Bayes classifiers often perform surprisingly well and are known for their ease of implementation, computational efficiency, and good results with small datasets. Their efficiency stems largely from the decoupling of the class conditional feature distributions, which means each distribution can be independently estimated as a one-dimensional distribution. This approach helps in handling missing data and reduces the risk of model overfitting, especially in cases where the number of observations is limited relative to the number of features [29].

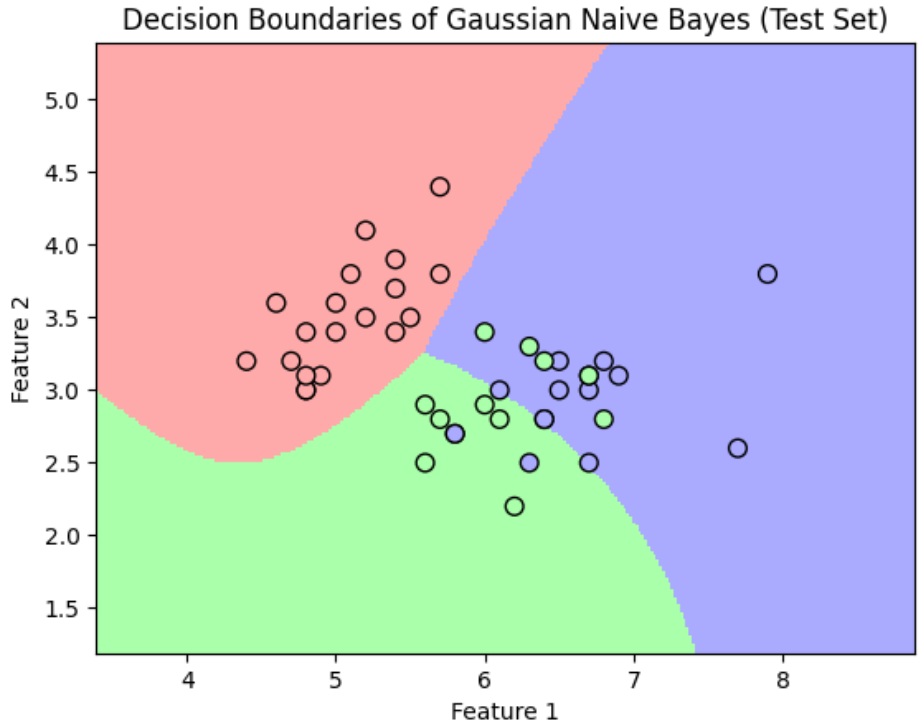

Figure 2.3 Naïve Bayes [30]

Random Forest Trees are an ensemble learning method, used for both classification and regression. This algorithm creates a 'forest' of decision trees and outputs the mode of the classes (classification) or mean prediction (regression) of the individual trees (Figure 2.4). Random forests correct for decision trees' habit of overfitting to their training set, providing more accurate results.

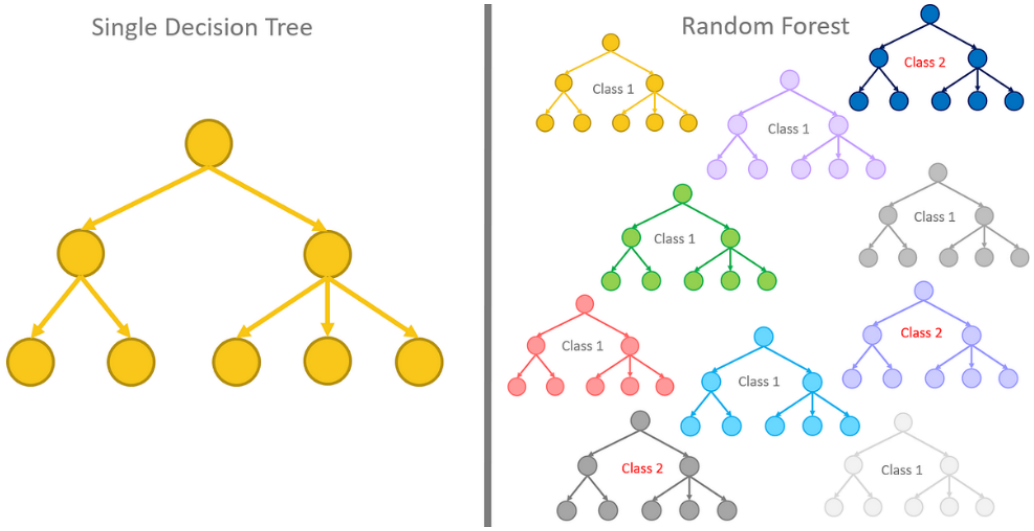

Figure 2.4 Random Forest Trees [31]

K-Nearest Neighbors (k-NN) is a simple, yet effective algorithm used for both classification and regression. In k-NN, the input consists of the k closest training examples in the feature space, and the output is a class membership or property value (Figure 2.5). The algorithm is highly versatile and can be used for a wide range of applications, from recommendation systems to pattern recognition.

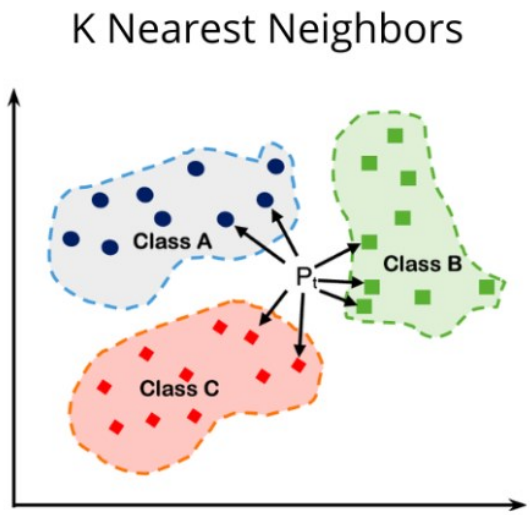

Figure 2.5 K-Nearest Neighbors (k-NN) [32]

Neural networks, the backbone of deep learning, are particularly useful for complex tasks like image and speech recognition. These networks mimic the workings of the human brain to process data, making them capable of learning nonlinear relationships.

The field of machine learning has witnessed considerable advances in recent years, particularly with the rise of deep learning and neural network architectures. Convolutional Neural Networks (CNNs) have revolutionized image processing, while Recurrent Neural Networks (RNNs) are pivotal in processing sequence data like language [33].

2.3. Deep Learning

The development of deep learning, particularly in the realm of Convolutional Neural Networks (CNNs), has seen remarkable advancements over the years, each marked by significant architectural innovations. These developments have progressively enhanced the performance and capabilities of CNNs in various applications, including image and

speech recognition, natural language processing, and more. This progression can be traced through several key architectures:

LeNet-5 (1998): As one of the earliest CNN architectures, LeNet-5 consists of two convolutional layers and three fully connected layers (Figure 2.6). Notably, it introduced what was then called a sub-sampling layer, now recognized as the average-pooling layer, featuring trainable weights. With approximately 60,000 parameters, LeNet-5 established a foundational template for CNN design: a structure that stacks convolutions and pooling layers, culminating in fully connected layers. This architecture marked a significant step in the evolution of CNNs [34].

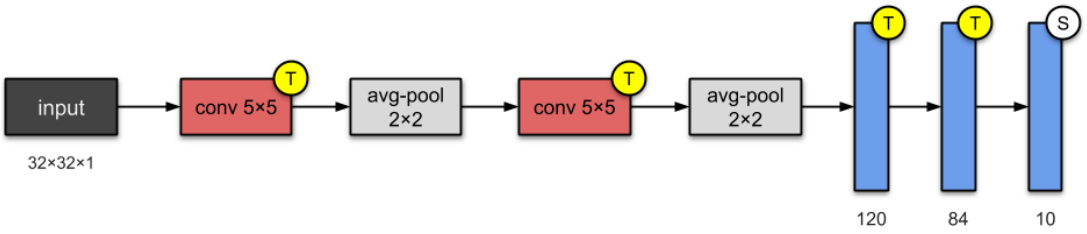

Figure 2.6 LeNet-5 architecture [35]

AlexNet (2012): Building upon the LeNet-5 framework, AlexNet comprises eight layers, including five convolutional and three fully connected layers (Figure 2.7). It is significantly larger, with around 60 million parameters, and introduced Rectified Linear Units (ReLUs) as activation functions. This innovation represented a pivotal advancement in deep learning, marking a departure from traditional activation functions used in neural networks [36].

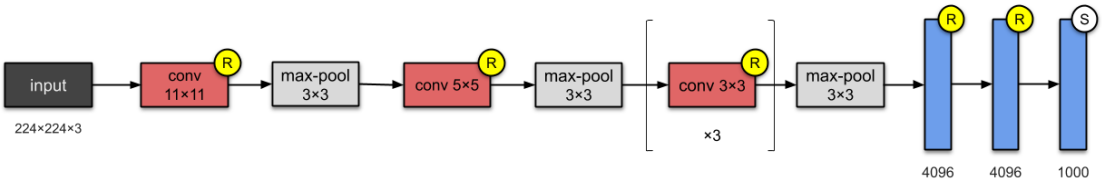

Figure 2.7 AlexNet architecture [35]

VGG-16 (2014): Extending the trend towards deeper architectures, VGG-16 features 13 convolutional layers and three fully connected layers, continuing the use of ReLU activation functions (Figure 2.8). The network employs more layers and smaller filter sizes, resulting in a model with 138 million parameters and approximately 500MB of

storage space. VGG-16 is notable for its approach to designing deeper networks through uniform convolutional stacking, approximately doubling the depth of AlexNet [37].

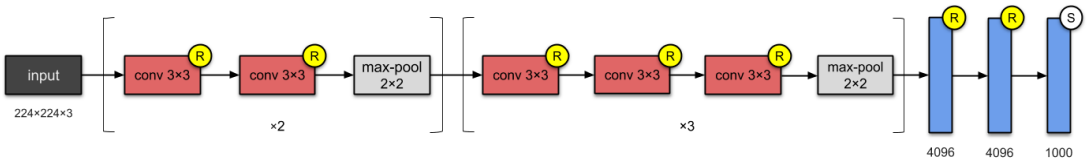

Figure 2.8 VGG-16 architecture [35]

Inception-v4 (2016): This architecture evolves from the Inception-v3, extensively incorporating the Network in Network principle through 'Inception modules' (Figure 2.9). These modules, a significant feature of the architecture, represent a shift from traditional convolutional layer stacking to stacking modules that contain convolutional layers. This approach is part of ongoing research on approximating sparse structures [38].

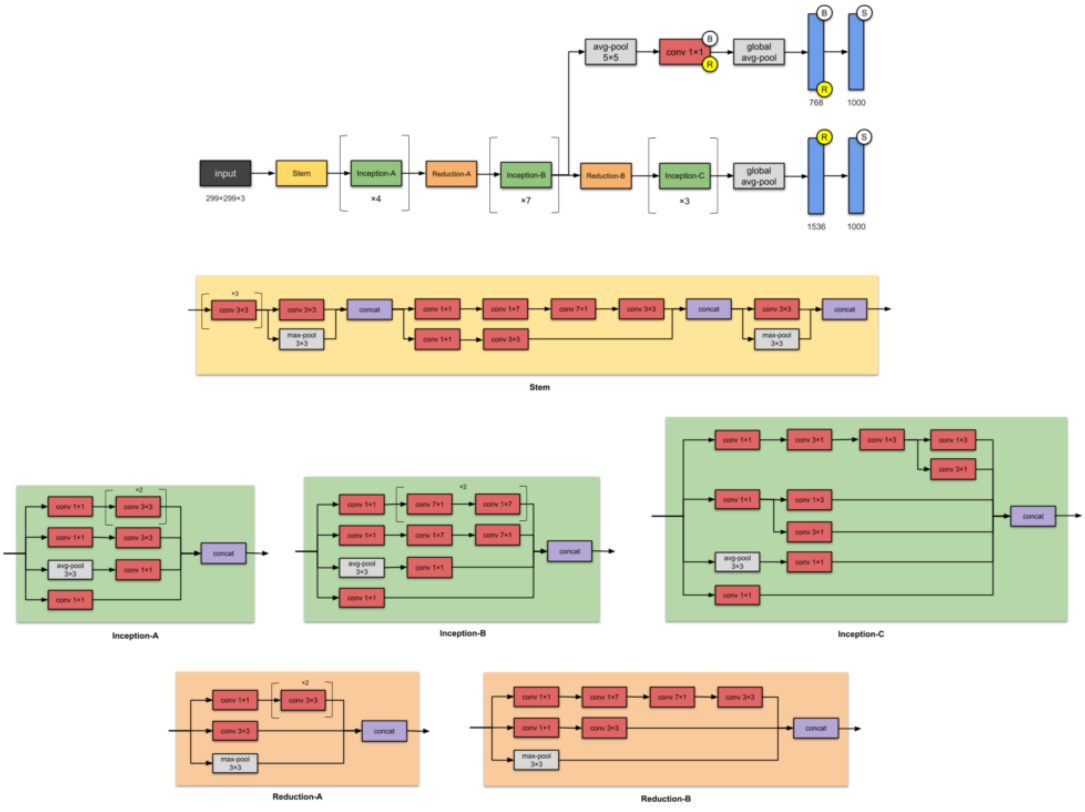

Figure 2.9 Inception-v4 architecture [35]

Xception (2016): A derivative of the Inception model, Xception replaces Inception modules with depth-wise separable convolutions (Figure 2.10). It maintains a similar parameter count to Inception-v1, approximately 23 million. The Xception model

exemplifies the trend of modifying and enhancing existing architectures to achieve improved performance [39], [40].

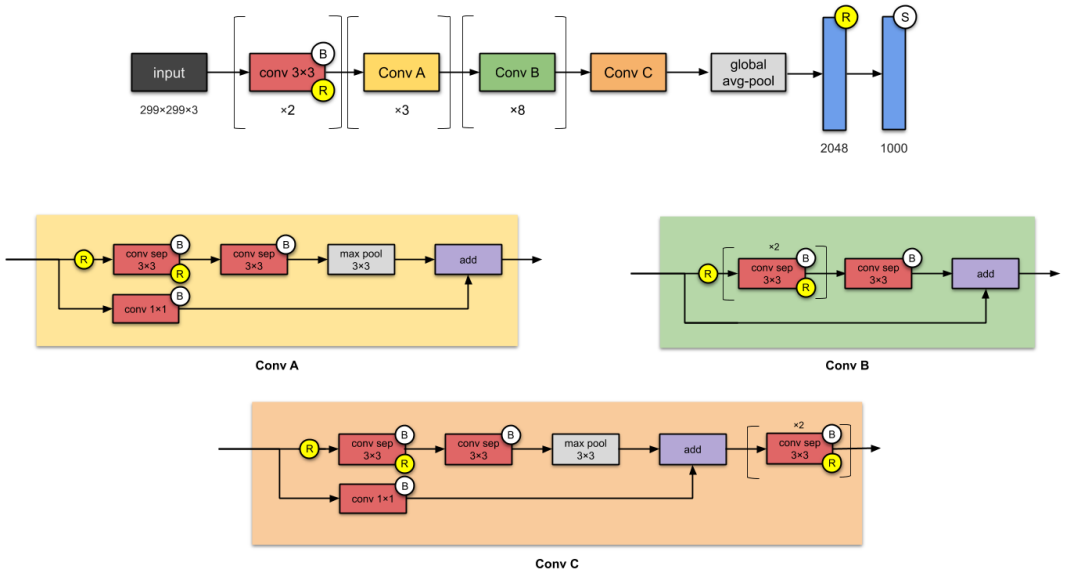

Figure 2.10 Xception architecture [35]

ResNet-50 (2015): Developed by Microsoft Research, ResNet-50 tackled the issue of accuracy degradation in very deep networks. It introduced skip connections in deeper models, helping to maintain performance even as network depth increased (Figure 2.11). Comprising 26 million parameters, ResNet was among the early implementations to include batch normalization, a technique that has since become a standard component in many deep learning architectures [41], [42].

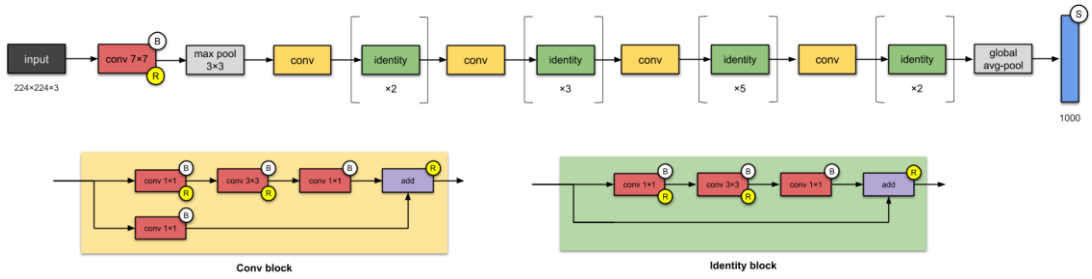

Figure 2.11 ResNet-50 architecture [35]

ResNeXt-50 (2017): With 25 million parameters, ResNeXt-50 differentiates itself from ResNet by incorporating parallel towers within each module (Figure 2.12). This design refines the model's ability to handle complex patterns and data structures, illustrating the

ongoing evolution in CNN design towards more sophisticated and capable architectures [43].

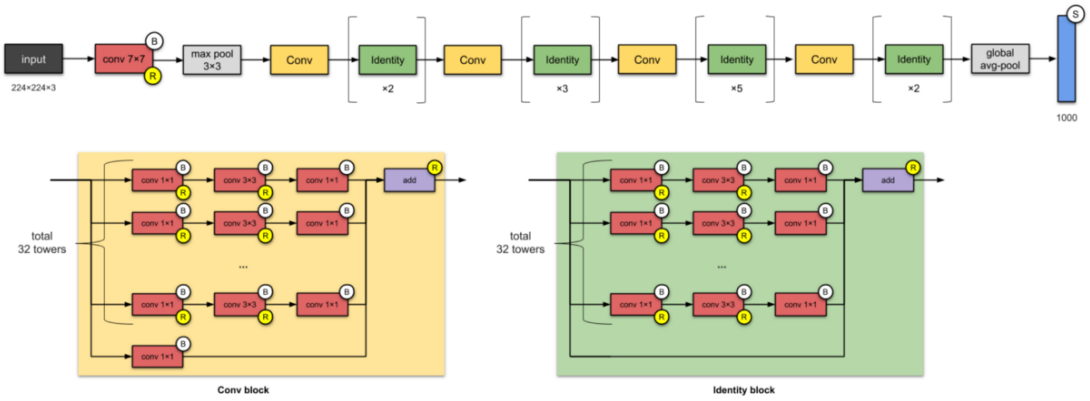

Figure 2.12 ResNeXt-50 architecture [35]

Convolutional Neural Networks (CNNs), another significant model that stands out is ResNet-101. This model is an extension of the ResNet architecture, which has been pivotal in advancing the field of deep learning.

ResNet-101 (2015): An extension of the ResNet-50 model, ResNet-101 deepens the architecture by incorporating 101 layers (Figure 2.13). It maintains the fundamental design principles of the original ResNet, including the use of skip connections, or residual connections, which help alleviate the vanishing gradient problem in deep networks. These connections allow the network to skip one or more layers, making it possible to train much deeper networks without a significant loss in accuracy [41].

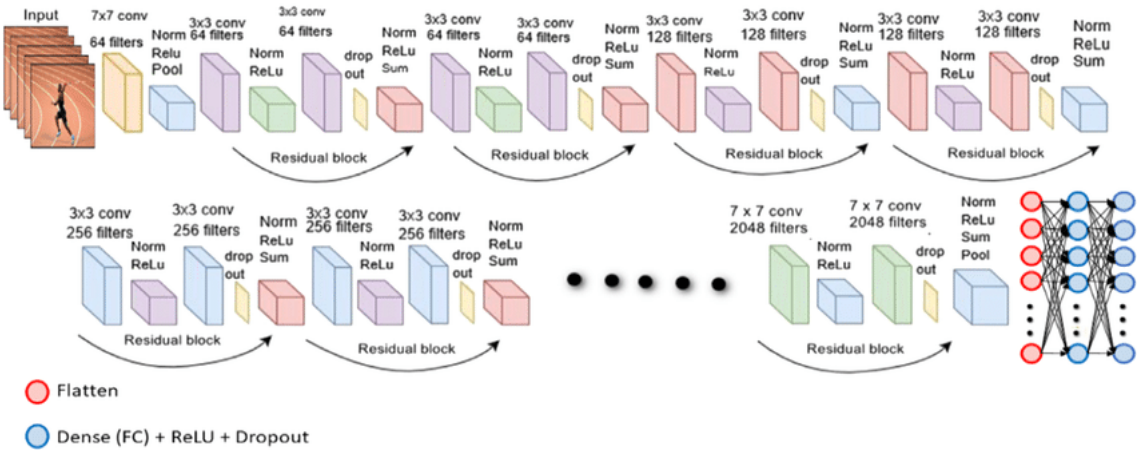

Figure 2.13 ResNet-101 architecture [44]

With 101 layers, ResNet-101 includes more convolutional layers compared to ResNet-50, enhancing its ability to learn more complex features and patterns. This increase in

depth translates to improved performance in various applications, particularly in tasks requiring fine-grained feature extraction, such as high-resolution image classification.

ResNet-101, like its predecessors, employs batch normalization, a technique that has become standard in deep learning models. Batch normalization helps in stabilizing the learning process and significantly reduces the number of training epochs required to train deep networks.

The introduction of ResNet-101 marked a significant milestone in the development of CNN architectures. It demonstrated the feasibility and effectiveness of building deeper neural networks, which was a challenging task before the advent of residual connections. The success of ResNet-101 has been influential in the design of subsequent deep learning models and architectures.

CHAPTER 3

STUDY-1

3.1. Classification and Analysis of Alzheimer's Disease Based on Changes of MRI Volumetric Features with Respect to Time

The clinical diagnosis of AD, while remaining the gold standard [9], has its limitations, necessitating the development of biomarkers capable of detecting early brain changes indicative of the disease. In this context, imaging techniques such as magnetic resonance imaging (MRI) and fluorodeoxyglucose positron emission tomography (FDG-PET) are increasingly utilized [45]. MRI, in particular, is adept at revealing brain anomalies associated with MCI and AD, potentially facilitating the differentiation between these conditions. Previous studies have utilized structural MRI for classifying AD and healthy subjects [46][47][48], while others have employed FDG-PET for similar purposes [49]. Möller et al. [50] investigated an MR image-based classifier to distinguish between AD and behavioral variant frontotemporal dementia, further exemplifying the precision achievable with MRI techniques. Additionally, Suk et al. [51] have used a fusion of multimodal information from MRI and PET, showcasing the breadth of neuroimaging applications in understanding neurodegenerative diseases. The integration of machine learning techniques has furthered this research, with functional MRI and convolutional neural networks (CNNs) being used to distinguish AD patients [52], and principal component analysis (PCA) and fuzzy logic applied in classification strategies [53][54].

Building upon these methodologies, our study introduces a unique perspective by focusing on the longitudinal changes in MRI volumetric parameters. This innovative approach utilizes the rate of change in brain volumes, and cortical thickness as features

for classification. Although previous studies have investigated brain volume changes in AD and MCI (e.g., Gispert et al. [55]), our research is pioneering in employing these dynamic changes as a basis for classification, thereby offering new insights into the progression of these neurological conditions.

Recent advancements in neuroimaging and computational analysis have emphasized the potential of MRI in elucidating the neurobiological underpinnings of Alzheimer's disease. Studies employing histogram-based features from MRI images have shown promise in tracking Alzheimer's progression, underscoring the importance of grey and white matter segmentation in understanding the disease's dynamics [56]. These techniques allow for the quantification of changes in tissue volume, informed by grey-to-white matter ratios, thus providing valuable insights into the gradual atrophy characteristic of AD [9]. A systematic review highlighted the growing application of machine learning techniques alongside neuroimaging data to predict the progression from MCI to AD. This review found structural MRI to be the most commonly used modality for this purpose, with studies increasingly integrating MRI data with other biomarkers and demographic information to improve prediction accuracy [47].

The integration of neuroimaging modalities and machine learning represents a significant stride toward the early detection and accurate classification of Alzheimer's disease and mild cognitive impairment. Research has shown that combining structural MRI with cerebrospinal fluid (CSF) data, neuropsychological assessments, and demographic information can enhance the predictive accuracy of models designed to identify individuals at risk of progressing from MCI to AD [57]. This integrative approach not only improves model performance but also offers a more comprehensive understanding of the disease's progression. Furthermore, the use of advanced imaging techniques, such as resting-state functional MRI (rs-fMRI), has demonstrated potential in classifying MCI converters-to-AD from non-converters with high accuracy by identifying affected brain regions.

Our investigation seeks to contribute to this growing body of knowledge by leveraging temporal changes in MRI volumetric parameters as a novel means of classifying AD, MCI, and healthy subjects. Through the lens of this research, we aim to bridge the gap in the literature by providing new insights into the early detection and nuanced understanding of Alzheimer's disease, paving the way for targeted interventions and

improved patient outcomes. This endeavor not only aligns with the latest scientific advancements but also pushes the boundaries of traditional diagnostic approaches, offering a fresh perspective on the capabilities of MRI technology in the context of neurodegenerative disease classification.

By situating our study within the context of these recent and relevant studies, we further the understanding of Alzheimer's disease and the potential of MRI as a diagnostic tool [58]. Our research contributes to the critical need for biomarkers for early detection, leveraging the advancements in imaging technology and computational analysis to offer a new avenue for diagnosing and understanding the progression of Alzheimer's disease and mild cognitive impairment.

The growing consensus in the scientific community is that early detection of Alzheimer's disease and the identification of individuals at risk for progression from MCI to AD are crucial for effective intervention and management. The integration of machine learning and MRI offers unprecedented opportunities in this regard, enabling the development of predictive models with the potential to transform clinical practice [59]. By focusing on the rate of change in MRI volumetric parameters over time, our study not only adds to the body of evidence supporting the use of neuroimaging biomarkers in the early detection of AD but also introduces a novel approach that could enhance the specificity and sensitivity of diagnostic procedures.

Moreover, the exploration of structural changes in the brain as a predictive tool for Alzheimer's disease progression represents a significant shift in the diagnostic paradigm. Traditional diagnostic methods, while effective, often diagnose the disease at a stage when therapeutic interventions are less likely to alter its course significantly. By providing a method to detect subtle changes over time, our research aligns with the broader goals of precision medicine, offering the possibility of personalized diagnostic and treatment strategies based on individual risk profiles and disease progression patterns.

This study represents a significant step forward in the automatic classification of Alzheimer's disease, mild cognitive impairment, and healthy subjects using MRI volumetric parameters. By harnessing the power of neuroimaging and machine learning, we aim to contribute to the early detection and understanding of Alzheimer's disease, ultimately improving patient care and outcomes. As we continue to explore the capabilities of MRI technology, the potential for significant advancements in the

diagnosis and treatment of neurodegenerative diseases becomes increasingly apparent, marking a promising direction for future research in this field.

3.2. Literature Review

Dhinagar et al. employed a deep learning approach on 3D T1-weighted brain MRI to classify Parkinson's disease (PD) and Alzheimer's disease (AD), conditions affecting millions globally. They assert that their 3D CNN model, with further validation, could assist in differentiating between AD and PD in cases where both diseases present similarly subtle motor and non-motor symptoms. However, their architecture utilized slices of 3D brain volumes rather than the whole volume [60].

Folego et al. explored deep learning methods to extract AD biomarkers from structural magnetic resonance imaging (sMRI) and classify brain images into AD, mild cognitive impairment (MCI), and cognitively normal (CN) groups. They adapted and trained Convolutional Neural Networks (CNNs) on sMRIs from online databases. Their method, ADNet, performed well in the CADDementia challenge, outperforming several existing approaches. The modified version with domain adaptation, ADNet-DA, achieved 52.3% accuracy. Their study's contributions include developing a fast, entirely automatic deep learning system that delivers competitive results without relying on domain-specific knowledge about the disease [61].

Khagi et al. segmented MRI using the Statistical Parameter Mapping (SPM) tool, applying a smoothing technique to obtain 3D grey matter images. These images were then processed through a 3D CNN to classify them as healthy control (HC), MCI due to AD (mAD), or AD dementia (ADD). While they used segmented information, the entire brain volume wasn't employed in the deep learning algorithm for classification [62].

Dyrba et al. investigated whether models with higher accuracy also depend more on discriminative brain regions defined by prior knowledge. They trained a CNN for AD detection using 663 T1-weighted MRI scans of dementia and amnestic MCI patients, verifying accuracy via cross-validation and in three independent samples totaling 1655 cases. They evaluated the association of relevance scores with hippocampus volume to validate clinical utility. They also implemented interactive 3D CNN relevance maps for model comprehensibility. The relevance maps indicated hippocampal atrophy as the most

informative factor for AD detection, supplemented by atrophy in other cortical and subcortical regions [63].

Mzoughi et al. proposed an efficient, fully automatic deep multi-scale 3D CNN architecture for glioma brain tumor classification into low-grade (LGG) and high-grade gliomas (HGG) using T1-Gado MRI sequences. This architecture utilizes small kernels to merge local and global contextual information with reduced weights. To address data heterogeneity, they implemented preprocessing techniques like intensity normalization and adaptive contrast enhancement. However, their technique processed MR images for CNN use, instead of using the entire brain volume in the CNN architecture [64].

Basnet et al. introduced a novel 3D DCNN architecture based on the U-Net structure for brain tissue segmentation into white matter, gray matter, and cerebrospinal fluid. Their method used densely connected convolutional layers and residual skip-connections to enhance representation capacity, improve gradient flow, facilitate learning, and reduce network parameters. They used cross-entropy, dice similarity, and a combination of both as loss functions for training. The approach yielded excellent performance on the IBSR18 and iSeg-2017 datasets while significantly reducing network parameters, employing both T1 and T2 weighted MR images in the CNN but not the entire brain volume [65].

3.3. Method

In this comprehensive study, we meticulously selected labeled MR images from the esteemed Alzheimer's Disease Neuroimaging Initiative (ADNI) database (adni.loni.usc.edu) [66], a pivotal resource in neuroimaging research. Our dataset comprised a carefully curated cohort of 22 cognitively normal (CN) individuals, 18 patients diagnosed with Alzheimer's Disease (AD), and 20 patients identified with Mild Cognitive Impairment (MCI). This diverse participant pool, with an average age of 76 years and an age range extending from 55 to 90 years, was instrumental in providing a broad perspective on the neurodegenerative spectrum encompassed by our research. Images of each patient were consisted of a yearly intervals.

A total of 351 MRI scans were included in our analysis, with a distribution of 129 scans from the CN group, 145 from the MCI group, and 77 from the AD group. These scans were obtained using 3T GE and Siemens MR machines, renowned for their precision and

clarity in imaging, over a span of three years. These scans were consisted of annually intervals. This temporal range allowed us to capture the progression and volumetric changes associated with Alzheimer's and cognitive decline with unparalleled detail.

The interval between consecutive scans varied among participants, yet most subjects underwent more than 5 scans, a frequency that enabled a comprehensive and longitudinal analysis of volumetric changes. This variability was meticulously accounted for in our study design, ensuring the reliability of our slope calculation methodology and mitigating the risk of overfitting. The strategic inclusion of multiple scans per subject not only enriched our dataset but also strengthened the foundation of our analysis, providing a robust framework for examining the nuanced volumetric trends indicative of neurodegenerative processes.

By leveraging the ADNI database's extensive repository of high-quality MR images and employing rigorous selection criteria, our study stands at the forefront of Alzheimer's research, offering novel insights into the volumetric biomarkers of disease progression and cognitive decline.

In our meticulous approach to feature extraction, the CAT12 toolbox [67], integrated within the Statistical Parametric Mapping (SPM) software [68] integrated in MATLAB [68], played a pivotal role. This choice was driven by CAT12's advanced capabilities in segmenting brain structures with exceptional precision (Figure 3.1), facilitating the extraction of volumetric values critical for our analysis, including white matter (WM), grey matter (GM), cerebrospinal fluid (CSF), total intracranial volume (TIV), and cortical thickness (CT). The utilization of the Montreal Neurological Institute (MNI) template [69] for normalization was strategic, ensuring that our data conformed to a standardized anatomical space, enhancing the comparability and reliability of our findings.

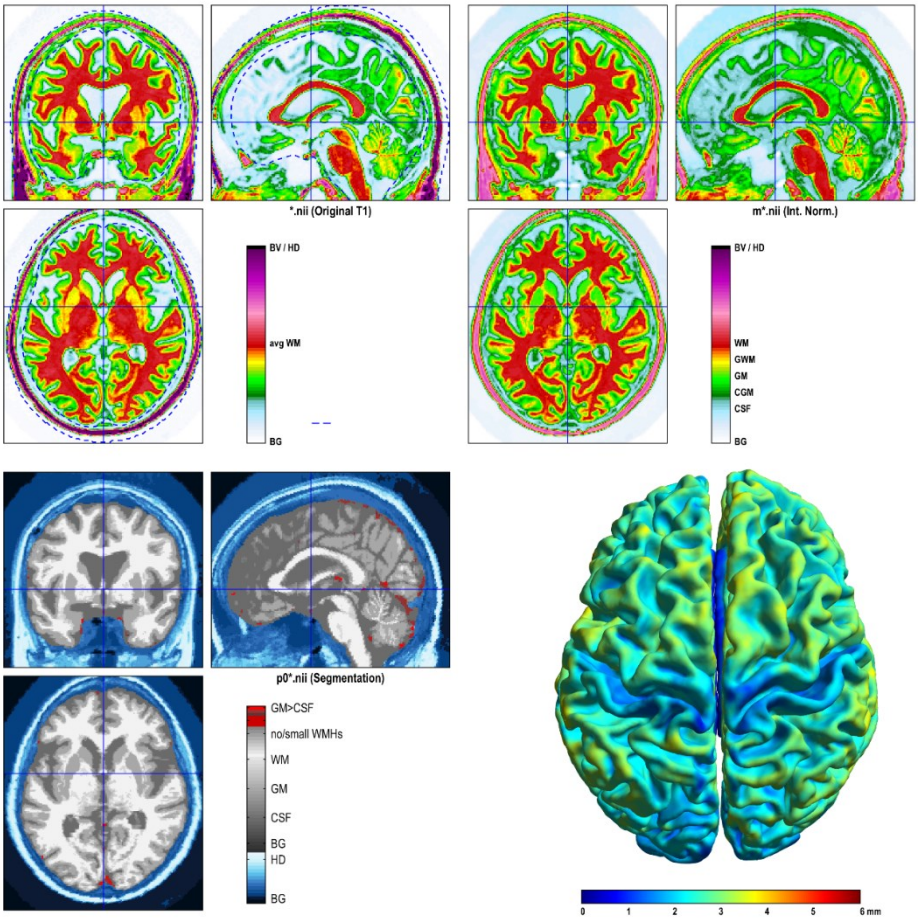

Figure 3.1 SPM output example of an AD patient

The segmentation process, crucial for delineating the brain's complex structures, allowed us to derive accurate volumetric measurements essential for understanding the neurodegenerative processes characteristic of Alzheimer's Disease and Mild Cognitive Impairment (Figure 3.2). By employing linear regression for line fitting across each subject's volumetric data over multiple scans, we captured the trajectory of volumetric changes with nuanced precision. This methodological choice, favoring linear over non-linear models, was predicated on the balance between simplicity and the robustness of capturing overarching trends in volumetric evolution. It acknowledges, however, the potential for non-linear models to provide deeper insights in future explorations.

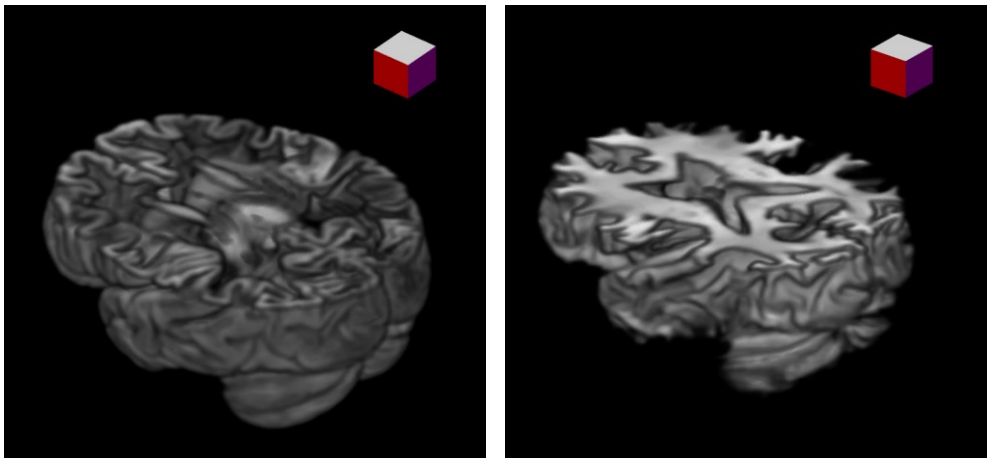

Figure 3.2 Segmentation output of white matter and grey matter of an AD patient

Subsequently, our analysis extended to computing the slopes of volumetric changes for TIV, WM, GM, CSF, and CT, using the time of scans (in days) and volumetric values as variables (Figure 3.3). This step was critical in quantifying the rate of neurodegeneration, offering a novel lens through which to view the progression of Alzheimer's Disease and related conditions. The slopes derived from this analysis did not merely represent statistical outputs; they embodied the dynamic and progressive nature of brain volume changes, setting the stage for the subsequent phase of our study where these features would be pivotal in machine learning classification.

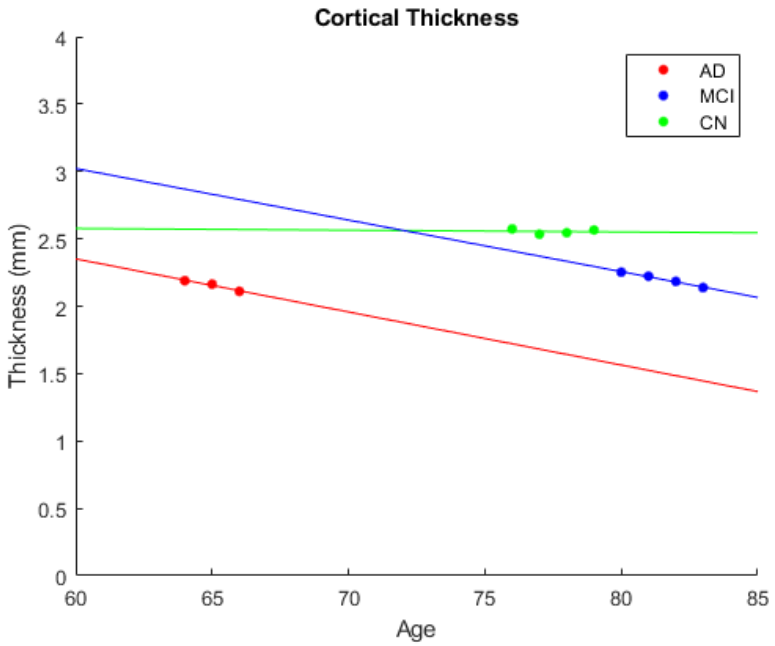

Figure 3.3 An example of fitted line for a patient from each group according to their CT

The features extracted were analyzed using IBM SPSS software (version 25). To examine the uniformity of changes in intracranial volumetric values, we focused on scans acquired approximately one year apart among different patient groups (CN, MCI, and AD), employing the Repeated Measures ANOVA technique [70]. This method is apt for assessing diseases at various time points. We conducted several statistical tests to identify the most discriminative features for classification, including multivariate tests, Mauchly's test of sphericity, Levene's test of equality of error variances, and Tukey's honestly significant difference (HSD) test.

Wilks' lambda test, utilized in ANOVA, assesses differences in mean vectors among identified groups [71]. A significance value below 0.05 ($p<0.05$) indicates a strong relationship between the predictor and criterion variables, while values closer to 1 suggest a weaker relationship. Mauchly's test checks for sphericity, with a significance value below 0.05 indicating a violation of assumptions for univariate tests [72]. Levene's Test of Equality of Variances evaluates homogeneity of variance, where a significance value above 0.05 suggests equal group variances [73]. Tukey's HSD test compares mean differences rather than individual pairs of values, with statistical significance denoted by values less than 0.05 [74].

The integration of these statistical tests, each contributing a unique lens through which to view our data, was pivotal in identifying the most discriminative MRI features for Alzheimer's disease classification. The calculated effect sizes, in tandem with p-values, afforded us a nuanced understanding of our findings' significance, guiding our interpretations and subsequent analytical decisions.

The integration of these statistical tests, each contributing a unique lens through which to view our data, was pivotal in identifying the most discriminative MRI features for Alzheimer's disease classification. The calculated effect sizes, in tandem with p-values, afforded us a nuanced understanding of our findings' significance, guiding our interpretations and subsequent analytical decisions.

In the pivotal classification phase of our research, we strategically harnessed the slope values indicative of the rate of change in intracranial volumes, alongside demographic variables such as gender and age, to fuel our machine learning models. This decision was rooted in the conviction that such features encapsulate crucial information on the

progression of Alzheimer's disease, thereby enabling the nuanced classification of AD, MCI, and CN groups.

We deployed Random Forest (RF) and Support Vector Machines (SVM) as our principal classifiers, esteemed for their robust performance in complex data landscapes. The RF model, celebrated for its resilience and versatility, was deemed particularly suitable for our dataset's varied volumetric changes. Its ability to navigate non-linear data and extract meaningful patterns from a multitude of scans made it a natural choice for our aims. In configuring the RF classifier, we set a random number generator seed at 1.0, ensuring a consistent starting point for model training. We also specified a minimum number of instances per leaf at 1.0, allowing the model to learn from even the smallest variations in data, and we did not cap the maximum depth of the trees, enabling them to grow until they had thoroughly learned the data.

Conversely, SVM was chosen for its unparalleled ability to discern intricate patterns within data, effectively managing the complex interplay between variables. The precision with which SVM handles high-dimensional data made it an invaluable tool in our classification arsenal. By fine-tuning the SVM parameters setting a complexity constant, a polynomial kernel exponent, and a gamma for the RBF kernel we meticulously calibrated the model to optimize its performance for our specific dataset.

Our utilization of the Waikato Environment for Knowledge Analysis (Weka) software further underscored our commitment to leveraging advanced tools for our analysis. Weka, with its extensive suite of machine learning algorithms, provided a robust platform for comparing the efficacy of our chosen classifiers [75]. The employment of stratified 10-fold cross-validation within Weka allowed for a rigorous evaluation of our models, minimizing variability, and bolstering the reliability of our findings.

This methodical approach to classification carefully selecting models, optimizing their parameters, and employing software for analysis—enabled us to navigate the complexities of our dataset. Through this process, we achieved a nuanced understanding of the models' performance, evaluating them against key metrics such as accuracy, sensitivity, specificity, and kappa values [76]. These metrics, widely recognized for their relevance in medical classification tasks, offered a comprehensive view of our models' capabilities, providing invaluable insights into their effectiveness in distinguishing between the different stages of cognitive decline.

3.4. Results and Discussions

Table 3.1 illustrates the mean and standard deviation values for each subject group and the volumetric features extracted using SPM software, complemented by age data.

Table 3.1 Means and standard deviations of the volumes and thicknesses for each group

Volumes and Thicknesses (mm^3 & mm)		Age	TIV	CSF	GM	WM	CT
AD	Mean:	75.42	1429.26	458.80	517.74	445.61	2.31
	Standard Deviation:	8.64	140.43	92.72	64.61	68.08	0.13
MCI	Mean:	75.20	1495.16	463.24	549.94	467.88	2.38
	Standard Deviation:	7.60	165.71	126.51	62.58	63.37	0.15
CN	Mean:	77.81	1422.12	419.76	544.01	451.39	2.45
	Standard Deviation:	4.11	158.32	141.00	37.01	38.73	0.12

The results from our statistical analysis indicated that the rate of change in cortical thickness (CT) was the most discriminative feature distinguishing AD patients from the cognitively normal group (CN). This was evidenced by the significance value (p-value) being less than 0.05 in Tukey's HSD and Wilk's Lambda tests (Table 3.2), while changes in CSF and TIV were not statistically significant.

Table 3.2 p values of statistical results

p values (within subjects and among groups)	Wilk's Lambda	Mauchly's Sphericity Test	Levene's Test	Tests of Between -Subject Effects	Tukey's HSD Test		
					AD-CN	AD-MCI	MCI-CN
Cortical Thickness	0.001	0.931	0.351	0.008	0.006	0.131	0.412
White Matter	0	0.429	0.070	0.346	0.959	0.364	0.493
Grey Matter	0	0.083	0.092	0.154	0.399	0.137	0.777
Total Intracranial Volume	0.081	0	0.830	0.258	0.993	0.314	0.344
Cerebrospinal Fluid	0.699	0	0.362	0.739	0.887	0.958	0.722

According to Tukey's HSD test (Table 3.2), the comparison of groups indicated that differentiating MCI from the AD and control groups was substantially more challenging

than distinguishing AD from the control group. Despite the rate of change in CT volume being the most distinct feature, it did not provide reliable discrimination on its own.

Upon inputting the mean CT volume values of each patient into our classifiers, we obtained the results as displayed in Table 3.3.

Table 3.3 Classification results according to the mean values of CT

Performance Measurement		Random Forest				Support Vector Machines			
		Acc.	Sens.	Spec.	Kappa	Acc.	Sens.	Spec.	Kappa
AD-CN		70%	72.7%	66.7%	0.39	67.5%	81.8%	50%	0.33
AD-MCI		57.9%	50%	65%	0.15	71.1%	61.1%	80%	0.42
MCI-CN		57.1%	59.1%	55%	0.14	66.7%	54.5%	80%	0.34
AD-MCI-CN	CN	41.7%	45.5%	53.6%	0.12	53.3%	50%	75%	0.30
	AD		44.4%	63%			27.8%	84.4%	
	MCI		35%	60%			80%	50%	

For classification purposes, alongside demographic information like gender and age, we utilized the slope of the lines (Table 3.4) fitted for each patient's CT volume. This was based on the observation that changes in CT volume showed the most significant statistical results in discrimination.

Table 3.4 Means and standard deviations of slope values of the volumes and thicknesses for each group

Slopes of Volumes and Thicknesses		Age	TIV	CSF	GM	WM	CT
AD	Mean:	75.42	0.01464	0.05730	-0.03115	-0.01363	-0.00012
	Standard Deviation:	8.64	0.12998	0.14151	0.02961	0.01711	0.00011
MCI	Mean:	75.20	0.03086	0.06303	-0.02298	-0.01238	-0.00008
	Standard Deviation:	7.60	0.08668	0.08820	0.03204	0.01523	0.00016
CN	Mean:	77.81	-0.01096	0.01107	-0.01286	-0.01155	-0.00001
	Standard Deviation:	4.11	0.11077	0.10537	0.01497	0.01679	0.00010

Employing the Random Forest (RF) classifier, we achieved an accuracy of 82.5%, sensitivity of 86.4%, and specificity of 77.8% in differentiating AD from CN. Conversely,

the Support Vector Machine (SVM) classifier yielded the best results in classifying MCI from AD and MCI from CN, with accuracies of 71.1% and 69.1%, respectively (Table 3.5).

Table 3.5 Classification results according to the slope values of CT

Performance Measurement		Random Forest				Support Vector Machines			
		Acc.	Sens.	Spec.	Kappa	Acc.	Sens.	Spec.	Kappa
AD-CN		82.5%	86.4%	77.8%	0.65	80.0%	78.8%	21.2%	0.11
MCI-AD		60.5%	63.4%	57.1%	0.21	71.1%	74.4%	66.7%	0.42
MCI-CN		66.7%	68.2%	65%	0.33	69.1%	71.1%	66.7%	0.39
AD-MCI-CN	CN	55%	59.1%	66.7%	0.32	53.3%	59.1%	64.5%	0.21
	AD		61.1%	71%			38.9%	92.9%	
	MCI		45%	75%			65%	58.8%	

When all three groups (AD, MCI, and CN) were classified together using Random Forest, we attained an overall accuracy of 55%.

In this first part of our study, we developed a methodology for the determination and automated classification of Alzheimer's Disease (AD). Our approach leveraged the rate of change in intracranial volumes over time as the key features for classification. Employing the Random Forest (RF) classification technique, we achieved an accuracy rate of 82.5% in distinguishing AD from the control/healthy group (CN).

Initially, we classified AD using all Magnetic Resonance (MR) scans from patients as independent scans. This approach yielded an accuracy of 91.5% with the k-nearest neighbors (kNN) algorithm and 87.2% with the RF method. With kNN, we successfully classified 116 CN subjects out of 129 (116/129), 71 AD patients out of 77 (71/77), and 134 MCI patients out of 145 (134/145). However, these results were somewhat misleading, as the classification was influenced by the memorization effect due to multiple scans from the same patients over different times.

Subsequently, we refined our approach by using mean values of the volumetric features of patients as input in the training and testing phases, resulting in the outcomes presented in Table 3.3. This adjustment offered more meaningful results compared to the initial stage of the study. A further enhancement was achieved when we employed the changes

in volumetric features (slopes of lines fitted to each patient's volumetric features) as inputs, which led to improved classification performance.

It was observed that the Total Intracranial Volume (TIV) parameter in AD patients decreased similarly to that in the MCI patients and control group. Additionally, the lack of significant changes in Cerebrospinal Fluid (CSF) volume was attributed to its calculation in SPM, which involved subtracting the sum of White Matter (WM), Grey Matter (GM), and Cortical Thickness (CT) volumes from TIV.

Our findings indicate that changes in CT volumes were the most effective feature for differentiating AD from CN, AD from MCI, and AD from CN and MCI patients. However, incorporating other volumetric features into the classification model led to a decrease in accuracy.

The most challenging aspect of this study was discriminating MCI cases. Even with the most effective classification feature, we only achieved an accuracy of around 70% when differentiating MCI from other groups.

Furthermore, we discovered that the rate of change in GM volume yielded better classification performance than that of WM volume in distinguishing AD patients from other groups. Notably, in the classification of AD and CN, including the rate of change in TIV alongside the rate of change in CT values resulted in a higher accuracy (85%) compared to using only the rate of change in CT values.

The findings of this study highlight the potential of MRI volumetric changes, particularly in cortical thickness (CT), as a biomarker for Alzheimer's Disease (AD). This aligns with established research identifying cortical atrophy as a critical indicator of neurodegenerative diseases. However, the transition from research findings to clinical applications involves several challenges and opportunities that need to be addressed to realize the practical utility of these insights.

The integration of MRI volumetric features into clinical practice requires validation through multi-stage clinical trials to ensure reliability and effectiveness in diverse patient populations. For instance, pilot studies should first verify the reproducibility of our findings in a controlled setting before broader clinical trials can evaluate the diagnostic accuracy in routine clinical use. Furthermore, integrating these volumetric measures into existing diagnostic frameworks could enhance the current AD diagnostic pathways,

which rely on cognitive assessments and basic neuroimaging. For example, adding a volumetric analysis module to MRI scans used in diagnostic settings could provide clinicians with quantitative data to support earlier and more accurate diagnoses.

In addition to the methodologies previously described, the choice of MRI parameters is crucial in the interpretation and reliability of our findings. The imaging parameters, such as field strength, voxel size, slice thickness, and scanning protocols, can significantly influence the accuracy of volumetric measurements and, consequently, the classification outcomes. For example, higher field strengths can enhance signal-to-noise ratios and resolution, allowing for more precise measurements of cortical thickness and other subtle changes associated with Alzheimer's disease. However, these parameters can also introduce variability in multi-site studies due to differences in MRI hardware and software configurations. To mitigate these issues and enhance the reproducibility of our results across different clinical settings, our study adheres to standardized imaging protocols modeled after the Alzheimer's Disease Neuroimaging Initiative (ADNI), which provides guidelines to harmonize MRI data collection [66]. Future studies should focus on further standardizing these parameters and exploring the impact of different MRI technologies, such as the use of 3T versus 7T scanners, on the diagnostic accuracy of Alzheimer's disease. Such considerations will be vital for translating MRI-based biomarkers from research environments into clinical practice, ensuring that our findings can be reliably replicated and applied in diverse healthcare settings.

In selecting MRI volumetric parameters for our study, we focused on cortical thickness and total intracranial volumes due to their proven sensitivity in detecting the subtle brain changes associated with Alzheimer's Disease (AD). Cortical thickness, in particular, is a robust biomarker that reflects neurodegenerative processes, a factor crucial in distinguishing between mild cognitive impairment (MCI) and more advanced stages of AD. The resolution, field strength, and sequence of the MRI scans were optimized to enhance the visualization of these parameters, with T1-weighted images commonly used for their high contrast between white and grey matter, facilitating accurate segmentation and measurement of cortical thickness.

However, these choices come with limitations. The accuracy of volumetric measurements can be significantly impacted by the MRI scanner's calibration and the specific imaging protocol used, which may vary across different clinical settings. Standardizing these

parameters is essential to ensure that data from different sources are comparable and that the findings are reproducible. Furthermore, while MRI offers detailed structural information, it lacks the functional data provided by PET scans, which can be crucial for a comprehensive understanding of AD pathology.

Validation of this MRI-based approach must address the standardization of imaging protocols across different settings to ensure consistent data quality. Variability in MRI scanners and imaging techniques can significantly affect the accuracy of volumetric measurements. Thus, developing standardized protocols for MRI scans and ensuring that these protocols are adhered to across various clinical environments is crucial. The ADNI protocols offer a foundation that could be adapted for broader clinical use.

Incorporating this methodology could significantly impact clinical outcomes by enabling earlier detection of AD and more precise monitoring of disease progression. By quantifying changes in cortical thickness, clinicians could potentially tailor interventions more effectively at an earlier stage of the disease, potentially slowing progression [77]. Moreover, the use of these quantitative measures could facilitate a more personalized approach to treatment, aligning with the goals of precision medicine in neurology.

The study acknowledges the modest sample size and the challenges this presents in terms of generalizability. Future research should aim to involve larger and more diverse populations to validate the applicability of these findings across different demographic and genetic backgrounds. Furthermore, exploring the integration of other biomarkers, such as genetic markers or additional neuroimaging data, could enhance the robustness and accuracy of the classification models.

By addressing these aspects, the transition of MRI volumetric analysis from a research tool to a clinical diagnostic aid can be significantly advanced, providing a valuable addition to the diagnostic arsenal against Alzheimer's disease. This discussion aims to bridge the gap between research findings and clinical application, offering a roadmap for future studies and implementation strategies.

Conclusively, our research makes a significant contribution towards elucidating AD classification via MRI volumetric features, spotlighting the criticality of cortical thickness. It lays the groundwork for future explorations that, by incorporating larger datasets, more equilibrated sample sizes, and a broader spectrum of features, could amplify the precision and reliability of this classification methodology. Such endeavors

promise a novel vista into understanding the progression of Alzheimer's Disease, heralding a more nuanced approach to its diagnosis and study. The incorporation of other biomarkers and clinical data could refine classification precision, acknowledging the constraints imposed by a predominant focus on CT alterations and the challenges posed by the relatively modest sample sizes, especially within the AD and MCI groups.

CHAPTER 4

STUDY-2

4.1. Time Distributed 3D CNN-LSTM Based Classification of Alzheimer’s Disease on MRI Scans

The progression to Study 2 in the thesis was driven by the need to address certain limitations encountered in Study 1 and to harness more advanced machine learning technologies that could provide deeper insights into the temporal dynamics of Alzheimer's disease. While Study 1 laid a solid foundation by utilizing traditional classification methods to analyze volumetric changes in MRI scans, it became evident that these methods were somewhat limited in capturing the complex, progressive nature of neurological changes associated with Alzheimer's and Mild Cognitive Impairment (MCI).

To overcome these limitations, Study 2 introduced a more sophisticated approach by integrating 3D Convolutional Neural Networks (CNNs) with Long Short-Term Memory (LSTM) networks. This combination was aimed at enhancing the model's ability to not only analyze spatial features within individual MRI scans but also to interpret these features over sequential scans, thereby capturing the temporal progression of the disease. This methodological enhancement was expected to improve the accuracy and reliability of predicting disease progression, providing a more robust tool for clinicians and researchers in the early diagnosis and monitoring of Alzheimer's disease. The shift to this advanced approach underscores a strategic move towards leveraging innovative AI technologies to better understand and predict the trajectories of neurodegenerative diseases.

In the realm of contemporary neuroimaging, the advent of advanced machine learning techniques, particularly deep learning, has precipitated a significant paradigm shift. This research aligns with this transformative trend, focusing on the application of these techniques to analyze 3D Magnetic Resonance Imaging (MRI) brain scans, with an emphasis on temporospatial dynamics [78]. At the core of our study lies the ambitious objective of leveraging temporal discrepancies across MRI scans to distinguish between Alzheimer's Disease (AD) patients, those with Mild Cognitive Impairment (MCI), and Cognitively Normal (CN) cohorts.

The impetus for this research is rooted in the critical role that early and accurate diagnosis plays in the management and understanding of AD. Alzheimer's Disease, a neurodegenerative disorder characterized by progressive cognitive and functional impairments, poses significant challenges to healthcare systems and society at large [1]. As the global population ages, the incidence of AD and other forms of dementia is expected to rise, amplifying the urgency for more effective diagnostic tools and treatment strategies.

MRI has emerged as a non-invasive diagnostic tool of choice in the study and analysis of AD, primarily due to its ability to provide detailed images of the brain's structure and function. It offers a window into the neurobiological underpinnings of the disease, capturing structural atrophies and pathological changes that are hallmarks of AD [79]. Moreover, advancements in MRI technology, such as functional MRI (fMRI), have further enhanced its utility, enabling the mapping of brain activity and offering insights into regions affected by the disease [80].

The integration of MRI with machine learning, and in particular deep learning, offers a new frontier in the diagnostic imaging of AD. Deep learning algorithms, particularly convolutional neural networks (CNNs), have demonstrated remarkable proficiency in image analysis, providing an automated and sophisticated approach to feature extraction from complex datasets [81]. These networks have shown significant promise in distinguishing between neurological conditions, offering a level of precision and accuracy that surpasses traditional methods [41].

An artificial neural network designed for handling sequential or time series data is known as a recurrent neural network (RNN) (Figure 4.1) [82]. These deep learning models are integral to well-known applications such as Siri, voice search, and Google Translate. They

are particularly effective for ordinal or temporal problems, including language translation, natural language processing (NLP), speech recognition, and image captioning.

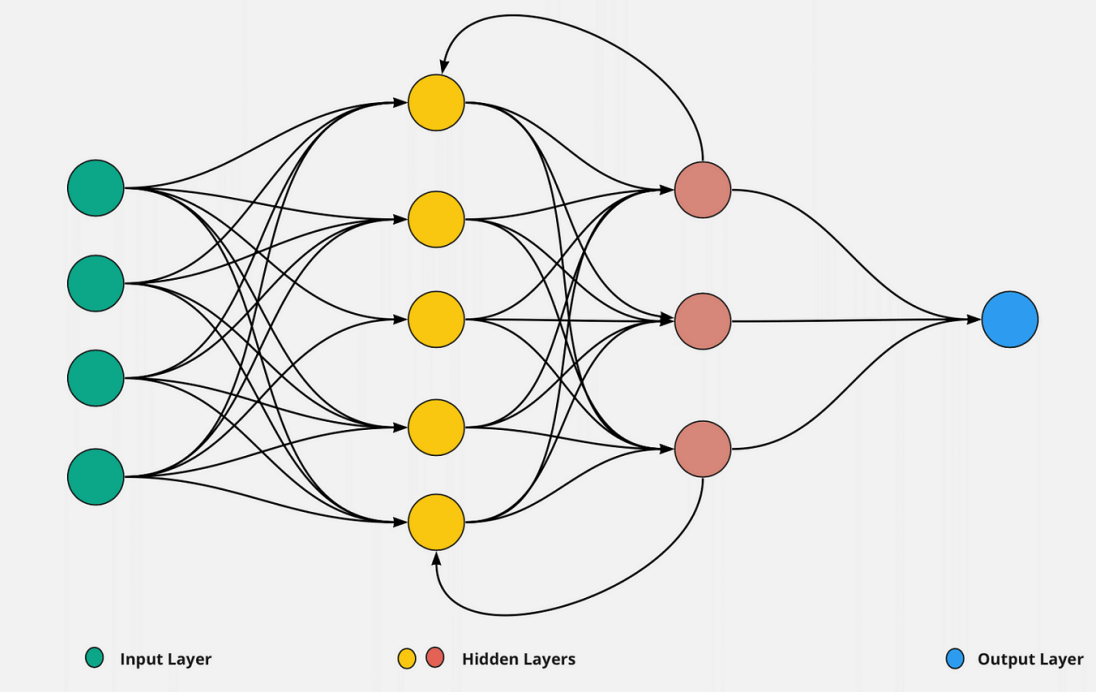

Figure 4.1 Recurrent Neural Network (RNN) [83]

Recurrent neural networks learn from training data, similar to feedforward and convolutional neural networks (CNNs). A distinctive feature of RNNs is their “memory”, which allows them to influence the current input and output using information from previous inputs. Unlike typical deep neural networks that assume inputs and outputs are independent of each other, the outputs of RNNs depend on preceding elements in the sequence [84]. Although accounting for future events could also enhance the accuracy of a sequence's output, unidirectional RNNs are unable to utilize future elements in their predictions.

The main distinction between CNNs and RNNs lies in the latter's ability to process temporal information. In contrast, the CNN LSTM architecture combines Convolutional Neural Network layers for extracting features from input data with Long Short-Term Memory (LSTM) units to enhance sequence prediction [85]. This hybrid model is particularly suited for visual time series prediction tasks and for generating textual descriptions from sequences of images and videos.

The critical difference between an LSTM unit and a standard RNN unit centers on the former's advanced design, which includes specialized gates—input, forget, and output

gates (Figure 4.2). These gates regulate the flow of information more effectively within the unit, enabling LSTMs to maintain and manage memory over longer sequences without suffering from the vanishing gradient problem that plagues standard RNNs. This capability makes LSTMs particularly suitable for tasks requiring the recognition of long-range dependencies, such as the classification of changes in MR images over time.

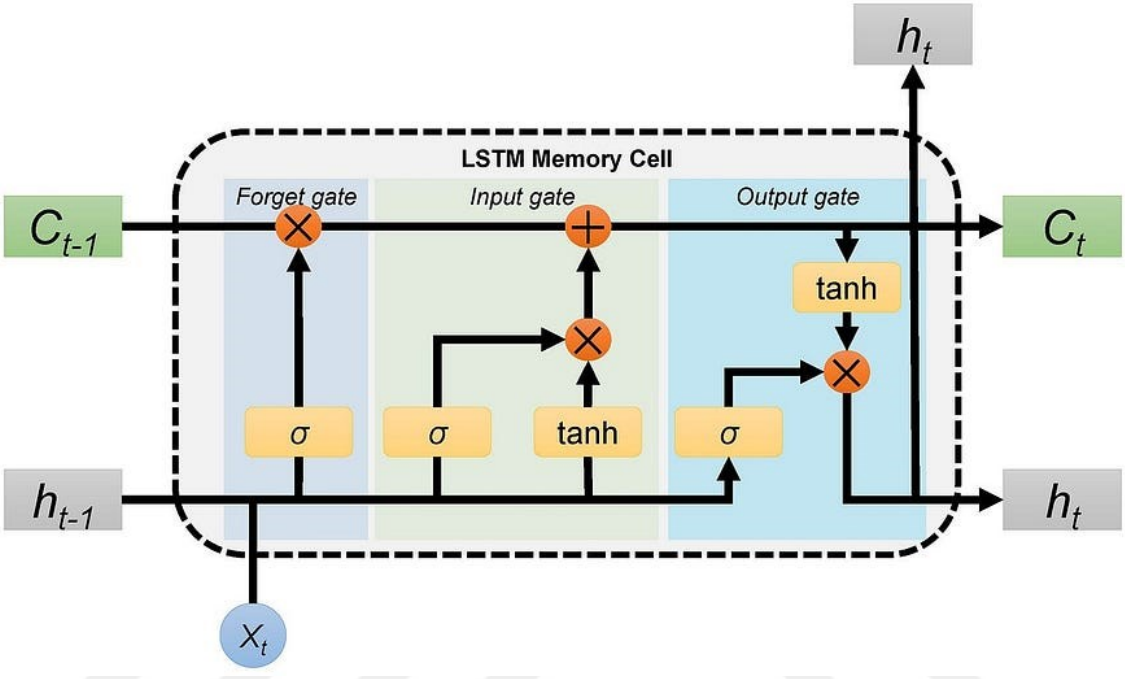

Figure 4.2 Typical representation of an LSTM layer [83]

Given the progressive nature of AD, the temporal aspect of the disease's evolution is critical. This is where Long Short-Term Memory (LSTM) networks come into play. LSTMs are adept at processing sequential data, making them particularly suitable for analyzing MRI scans taken over time. They are capable of capturing the longitudinal changes in the brain's structure and function, which are indicative of the progression or onset of AD [86].

The combination of CNNs and LSTMs in this research aims to harness both the spatial and temporal information present in sequential MRI scans (Figure 4.3). While CNNs extract salient features from individual MRI images, LSTMs analyze these features across time, providing a comprehensive view of the disease's progression [87]. This approach is anticipated to offer significant insights into the early detection and staging of AD, potentially leading to more timely and targeted therapeutic interventions [88].

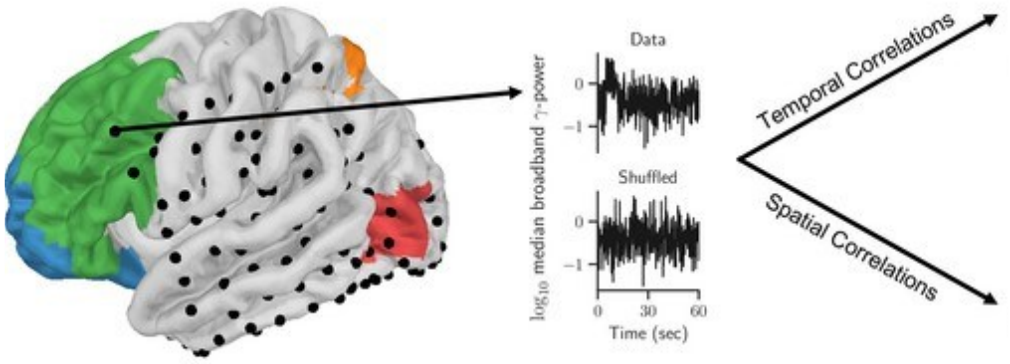

Figure 4.3 Symbiotic alliance of spatial-temporal analyses [89]

In conclusion, this study represents a confluence of innovative machine learning techniques and neuroimaging, aiming to provide a deeper understanding of Alzheimer's Disease. By leveraging the spatial and temporal capabilities of CNNs and LSTMs, respectively, it strives to contribute to the evolving landscape of AD diagnosis and management, offering hope for more effective and personalized care strategies for individuals affected by this challenging condition.

4.2. Literature Review

Deep learning, especially convolutional neural networks (CNNs), has redefined the possibilities in neuroimaging analysis. They offer automated, hierarchical feature learning and have demonstrated superior performance in image classification tasks, including the differentiation of neurological conditions [78]. A pivotal example is the convolutional neural network trained on more than a million images from the ImageNet database [90]. ImageNet is an image database organized according to the WordNet hierarchy [91], which provides a robust foundation for developing high-performance models that can effectively process and analyze medical imaging data .

MRI has been pivotal in the investigation of Alzheimer's disease, capturing structural atrophies, and patterns typical of the disease's progression [79]. Functional MRI (fMRI)

provides further granularity, highlighting regions with decreased activity. Studies have underscored MRI's capacity to detect early AD hallmarks, making it invaluable for timely interventions [80].

With advancements in CNN architectures, studies have effectively utilized models like ResNet for classifying MRI images, providing enhanced accuracy in distinguishing AD cases from healthy controls [81].

LSTMs have been employed in various neuroimaging studies, especially when sequences of data, like time-series or successive scans, are involved. Their inherent design is adept at handling long-term dependencies, making them suitable for analyzing the temporal evolution of neurological conditions [92].

There is a burgeoning interest in hybrid models that couple the spatial proficiency of CNNs with LSTMs' temporal sensitivity. Such amalgamations capitalize on CNNs' feature extraction capabilities, feeding these into LSTMs to glean insights from sequential data [87]. Notably, this approach aligns with studies where patients undergo multiple MRI sessions over extended periods, enabling a richer, temporally-informed understanding of disease progression [88].

The complexity of video quality assessment (VQA) stems from modeling perceived quality in both spatial and temporal dimensions. A novel no-reference (NR) video quality metric (VQM) is introduced, integrating 3D convolution neural network (3D-CNN) and LSTM units. The 3D-CNNs extract local spatiotemporal features from video clips, which the LSTM network then uses to predict video quality. This design effectively addresses the issue of limited training data and captures quality characteristics efficiently. Testing on two public video quality datasets revealed the proposed metric's superiority over other NR quality metrics [93].

The study of Montaha et al. [94] employed three BraTS MRI datasets from 2018, 2019, and 2020, aiming to differentiate between high-grade (HGG) and low-grade gliomas (LGG). These datasets consisted of four MRI sequences per patient. A hybrid model, TimeDistributed-CNN-LSTM (TD-CNN-LSTM), was proposed, which utilized all four 3D MRI sequences collectively as input. Another approach used a separate 3D CNN for each MRI sequence. The results indicated the TD-CNN-LSTM model surpassed the 3D CNN, achieving a test accuracy of 98.90%.

The study of Ebrahimi et al. [95] focused on enhancing Alzheimer's disease (AD) detection from MRI images using convolutional neural networks (CNNs). By comparing various deep learning models, including 2D and 3D CNNs and recurrent neural networks (RNNs), the research identified the limitations of using 2D slices in capturing MRI volume relationships. To address this, a hybrid model combining 2D CNNs with RNNs was proposed, ensuring the sequence of MRI slices was taken into account. However, the most promising results came from a voxel-based 3D CNN approach that employed transfer learning from a 2D image dataset. This method achieved an impressive 96.88% accuracy in distinguishing AD patients from healthy subjects, highlighting the potential of 3D CNNs and transfer learning in the early detection of AD.

4.3. Method

In this last phase of our study, we aimed to harness sophisticated deep learning paradigms to analyze 3D Magnetic Resonance Imaging (MRI) brain scans, emphasizing the temporospatial dynamics. The primary objective centered on utilizing the temporal discrepancies evident across MRI scans to delineate between Alzheimer's Disease (AD) patients, Cognitively Normal (CN) cohorts and Mild Cognitive Impairment (MCI).

MRI datasets, mentioned in the phase 1, curated in the rigorous Neuroimaging Informatics Technology Initiative (NIfTI) format, formed the foundation of this research. Each participant underwent a series of MRI scans, typically encompassing 3 or 4 sessions, conducted at annual intervals. This selected methodical, temporal spacing was anticipated to capture the nuanced neurobiological transitions manifesting within the cerebral architecture.

The classification has been achieved in between; AD-CN, CN-MCI, and AD-MCI. We have used binary classification since the pre-trained model has been designed for 2 classes: CN and AD patients.

MRI data was diligently cataloged within a structured Excel matrix. Ensuring each patient's scans were grouped, preserving the chronological order to emphasize the temporal evolution. All images were resized to a consistent 224 x 224 x 224 pixels, ensuring uniformity for the pre-trained neural network. The images for each patient were structured into sequences, reinforcing the time-differentiated analysis focus.

For spatial feature extraction, we employed a pre-trained 3D ResNet-101 architecture [95]. Importantly, this architecture's output, specifically, the extracted feature vectors, became the critical input for subsequent computational layers. To address the temporal intricacies inherent to the dataset, Long Short-Term Memory (LSTM) layers were integrated (Figure 4.4). LSTMs, renowned for their sequential processing capabilities, were pivotal in elucidating the longitudinal patterns inherent in the MRI acquisitions.

Thus, the architectural synthesis encapsulated a dual focus: Convolutional Neural Networks (via ResNet) for spatial delineation, and LSTM for longitudinal trajectories. While the CNN paradigm excavated spatial nuances within each scan, the LSTM framework synthesized these insights over temporal intervals, tracing the neurobiological evolution.

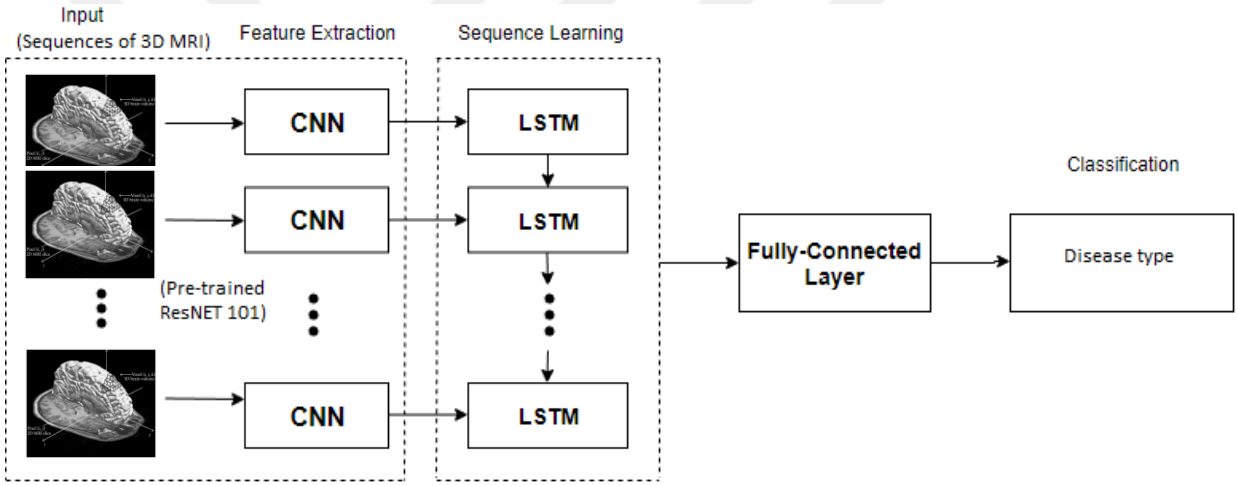

Figure 4.4 Designed LSTM-CNN network [96]

4.4. Results and Discussions

The training parameters employed in this study pertained to a pre-trained 3D Convolutional Neural Network (CNN) architecture. These parameters encompassed a maximum number of training epochs set at 30, an initial learning rate of 0.0001, and L2 regularization with a coefficient of 0.005. The utilization of a mini-batch size of 8 was necessitated by the available computational resources. During training for the classification task of Alzheimer's Disease (AD) and Cognitively Normal (CN) subjects, a piecewise learning rate schedule was implemented, incorporating a learning rate drop

factor of 0.1 and a drop period of 5 epochs. This strategy aimed to gradually reduce the learning rate for the pre-trained AD-CN network.

However, it is worth noting that an initial learning rate of 0.0003 was employed when classifying Mild Cognitive Impairment (MCI) subjects against CN and AD subjects. This adjustment was necessary because the pre-trained network had not been specifically trained for MCI classification; it had been trained exclusively for AD and CN classification. The optimization algorithm chosen was Stochastic Gradient Descent (SGD) with a momentum term of 0.9, and early stopping was implemented based on the performance assessed on a validation set.

Furthermore, the same training parameters were applied consistently across all Long Short-Term Memory (LSTM) models, which included a mini-batch size of 64, an initial learning rate of 0.01, and L2 regularization with a coefficient of 0.0001. SGD with a momentum term of 0.9 served as the optimizer, and the maximum number of training epochs was limited to 30, with early stopping based on validation set performance. Although the temporal order of data was considered crucial for capturing temporal patterns, the data shuffling option was explicitly set to 'never' to preserve the sequential order of the data samples during training.

Initially, we categorized AD-CN, AD-MCI, and CN-MCI using the first images of each patient through the pre-trained 3D ResNet-101 CNN algorithm, which based its decisions on the entirety of the MRI volume. The 3D CNN not only extracted features from individual image volumes but also discerned the relationship between sequential images for each patient. Subsequently, we utilized an LSTM to process sequences of images (comprising 3 or 4 annual shots) for each patient. The classification results, with averages and standard deviations from 10 iterations, are presented in Table 4.1.

Table 4.1 Means and standard deviations of LSTM-CNN & CNN classification accuracies

Accuracy (10 iteration)	CNN (First image)			LSTM-CNN (Sequences of 3-4 images taken annually)		
	AD-CN	AD-MCI	CN-MCI	AD-CN	AD-MCI	CN-MCI
Mean	90.4	78.3	76.5	96.7	87.5	86.4
Std. Deviation	3.17	3.93	3.64	2.97	3.77	3.35

By incorporating the LSTM and temporal data, we achieved a 96.7% accuracy rate, enhancing our ability to differentiate between AD and CN by 6%. The accuracy in distinguishing AD-MCI from MCI-CN surged by 10% when factoring in the temporal information. The subpar accuracy in MCI classification stems from the pre-training of the model on CN and AD patient data. Our model was unable to increase accuracy of MCI because of limited number of annually taken 3D MRI data.

CHAPTER 5

CONCLUSION AND FUTURE PROSPECTS

5.1. Conclusion

Alzheimer's disease (AD), as the most prevalent form of dementia, presents a critical challenge in modern medical science. Its early detection is essential for managing the disease's progression in the absence of a definitive cure. This study represents a significant stride in this direction, aiming to establish an innovative methodology for the automatic classification of AD. By focusing on the temporal variations in MRI volumetric parameters, the research sought to harness these changes as key features in distinguishing between AD, Mild Cognitive Impairment (MCI), and Cognitively Normal (CN) individuals.

The first phase of the study marks a significant advancement in the utilization of temporal alterations in MRI volumetric attributes for discerning AD, MCI, and the status of healthy control subjects. Through the meticulous analysis of 351 MRI scans sourced from the Alzheimer's Disease Neuroimaging Initiative database, this study illuminates the pivotal role of cortical thickness (CT) rate of change as a fundamental discriminative marker. Notably, alterations in CT have demonstrated remarkable efficacy in differentiating AD from healthy subjects, achieving an accuracy of 82.5% utilizing the Random Forest classification method.

The endeavor to accurately segregate MCI from AD and healthy controls, however, encountered hurdles, with SVM classification accuracies approximating 70%. This underlines the diagnostic challenges associated with MCI, characterized by its nuanced and fluctuating symptoms. The study openly acknowledges limitations, such as sample

size and the temporal distribution of scans, which may affect the extrapolation of the results.

The study then progressed to its second phase, which involved the integration of a pre-trained 3D ResNet-101 CNN algorithm with Long Short-Term Memory (LSTM) networks significantly enhanced the methodology. By processing sequences of 3 or 4 annual scans for each patient, LSTM networks were able to capture the subtle temporal changes in brain volumetrics that are crucial for accurate diagnosis. This methodological advancement led to remarkable improvements in classification accuracy: achieving 96.7% in distinguishing AD from CN subjects, 87.5% in differentiating AD from MCI, and 86.4% in separating MCI from CN subjects. The results clearly underscore the superior capability of LSTMs to utilize temporal information, providing a robust basis for more accurate classification of Alzheimer's disease progression compared to earlier phases that relied on traditional methods.

In conclusion, this study underscores the potential of a combined CNN and LSTM approach in neuroimaging for Alzheimer's disease. By leveraging the temporal dynamics of MRI volumetric parameters, the research provides a nuanced perspective on AD classification. The findings demonstrate the value of temporal changes as robust features in enhancing the early detection and comprehensive understanding of Alzheimer's disease. This approach could lead to more timely and targeted interventions, significantly contributing to the field of neurodegenerative disease research and offering new avenues for patient care.

5.2. Contribution to Global Sustainability

Alzheimer's disease (AD), recognized by the World Health Organization (WHO) as a principal cause of dementia, affects approximately 50 million individuals globally, with numbers expected to increase as populations age [3]. Our study's contributions towards global sustainability in the context of this growing health challenge are multifaceted.

Firstly, early detection and accurate classification of Alzheimer's disease, as facilitated by our research, are crucial for improving patient outcomes. By enabling timely interventions, our approach aids in decelerating disease progression, enhancing the quality of life for patients, and reducing the caregiver and healthcare system burdens.

Secondly, the economic implications of dementia, including AD, are substantial, with global costs exceeding US$ 1 trillion annually, as reported by the WHO [3]. By potentially reducing long-term healthcare expenditures through improved diagnostic methods, our research contributes to economic sustainability.

Furthermore, the societal impact of Alzheimer's disease is profound, exerting significant psychological, emotional, and financial strains on families and communities. Our study's emphasis on earlier and more accurate diagnosis supports better disease management, thus alleviating its social impact. In addition, the methodologies and findings from our research contribute to the advancement of medical science, particularly in neuroimaging and machine learning. This contribution is pivotal in expanding the knowledge base in neuroscience and geriatric medicine, laying the groundwork for future research initiatives.

Lastly, our research underlines the importance of technological advancements in addressing global health challenges and supports the development of health policies focused on early detection and management of dementia. By highlighting the effectiveness of integrating machine learning with neuroimaging for AD diagnosis, it also raises global awareness of the potential for technology to address critical health issues.

In summary, our study offers significant contributions to the global sustainability efforts in public health, economic stability, social welfare, medical research, and health policy, particularly in the context of addressing the challenges posed by Alzheimer's disease.

5.3. Future Prospects

Looking forward, it is essential for future research to aim at broadening the scope of investigation by increasing the sample size and diversifying the range of volumetric attributes analyzed. This expansion will undoubtedly bolster the robustness and reliability of the classification models. Furthermore, the incorporation of advanced, non-linear statistical methods is expected to sharpen the accuracy and enhance the predictive capabilities of these models. Extending this integrated CNN-LSTM methodology to other neurodegenerative disorders could also yield significant breakthroughs, offering new perspectives on their progression patterns and making substantial contributions to the domain of medical imaging and patient care. This broader application promises to

enhance diagnostic frameworks and treatment strategies, ultimately improving outcomes across a spectrum of neurodegenerative diseases.

Building upon the significant advancements made in this study, several promising prospects emerge that could shape the future landscape of neuroimaging and machine learning in Alzheimer's disease diagnosis.

The integration of SPM-segmented White Matter (WM) and Gray Matter (GM) outputs from 3D MRI scans into CNN-LSTM architectures offers a promising prospect. This approach could lead to more sophisticated diagnostic models, providing finer details and a deeper understanding of AD progression, thereby aiding clinicians in early and accurate diagnosis.

Utilizing feature vectors derived from pre-trained 3D CNNs in various machine learning algorithms presents an opportunity to develop hybrid diagnostic tools. These tools could significantly enhance classification accuracy, leading to better differentiation between AD, MCI, and CN, potentially influencing treatment strategies and patient care.

In addition to these specific research directions, the future prospects also extend to the potential impact on clinical practices. The advancements in automated and precise diagnostics could pave the way for personalized medicine approaches in neurodegenerative diseases. Moreover, the integration of these advanced computational techniques in medical imaging could also spur technological innovations, leading to new tools and software for healthcare providers.

Furthermore, as our understanding of Alzheimer's disease deepens through such research, there is an opportunity to influence public health policy. With early and accurate diagnosis becoming more achievable, healthcare systems can better allocate resources and plan interventions, ultimately contributing to the global effort in managing and mitigating the impact of Alzheimer's disease.

These prospects highlight the multidimensional impact of the current research, extending beyond academia into clinical, technological, and policy-making realms, reinforcing the critical role of advanced research in shaping the future of healthcare and public health.

BIBLIOGRAPHY

[1] Alzheimer's Association and A. Association, "2009 Alzheimer's disease facts and figures," *Alzheimer's Dement.*, vol. 5, no. 3, pp. 234–270, 2009, doi: 10.1016/j.jalz.2009.03.001.

[2] R. B. M. Prince and C. Ferri, "Alzheimer's disease international. World Alzheimer Report." King's College London London, UK, 2011.

[3] WHO; World Health Organization and Alzheimer's Disease International, "Dementia: a public health priority," p. 102, 2012, Accessed: Nov. 14, 2023. [Online]. Available: https://apps.who.int/iris/bitstream/handle/10665/75263/9789241564458_eng.pdf.

[4] National Institute on Aging, "Alzheimer's Disease Fact Sheet Alzheimer's Disease Fact Sheet," *National Institute on Aging*. Washington, DC: US Department of Health and Human Services.[Google Scholar], pp. 1–8, 1900, [Online]. Available: https://www.nia.nih.gov/health/alzheimers-disease-fact-sheet.

[5] J. C. Morris, "Alzheimer's Disease and Mild Cognitive Impairment," *Handb. Dementing Illnesses, Second Ed.*, vol. 25, no. 3, pp. 191–208, 2006, doi: 10.3109/9780849354847-14.

[6] R. Petersen, "Early Diagnosis of Alzheimers Disease: Is MCI Too Late?," *Curr. Alzheimer Res.*, vol. 6, no. 4, pp. 324–330, 2009, doi: 10.2174/156720509788929237.

[7] R. Brookmeyer, E. Johnson, K. Ziegler-Graham, and H. M. Arrighi, "Forecasting the global burden of Alzheimer's disease," *Alzheimer's Dement.*, vol. 3, no. 3, pp. 186–191, 2007, doi: 10.1016/j.jalz.2007.04.381.

[8] C. P. Ferri *et al.*, "Global prevalence of dementia: A Delphi consensus study," *Lancet*, vol. 366, no. 9503, pp. 2112–2117, 2005, doi: 10.1016/S0140-6736(05)67889-0.

[9] A. Lim *et al.*, "Clinico-neuropathological correlation of Alzheimer's disease in a community-based case series," *J. Am. Geriatr. Soc.*, vol. 47, no. 5, pp. 564–569, 1999, doi: 10.1111/j.1532-5415.1999.tb02571.x.

[10] T. G. Beach, S. E. Monsell, L. E. Phillips, and W. Kukull, "Accuracy of the clinical diagnosis of Alzheimer disease at National Institute on Aging Alzheimer Disease Centers, 2005-2010," *J. Neuropathol. Exp. Neurol.*, vol. 71, no. 4, pp. 266–273, 2012, doi: 10.1097/NEN.0b013e31824b211b.

[11] B. Gómez-Ansón, "Advances in neuroimaging in Alzheimer's disease and other dementias," *Riv. di Neuroradiol.*, vol. 18, no. 4, pp. 469–477, 2005, doi: 10.1177/197140090501800407.

[12] L. Mosconi, M. Brys, L. Glodzik-Sobanska, S. De Santi, H. Rusinek, and M. J. de Leon, "Early detection of Alzheimer's disease using neuroimaging," *Exp. Gerontol.*, vol. 42, no. 1–2, pp. 129–138, 2007, doi: 10.1016/j.exger.2006.05.016.

[13] C. L. Masters, R. Bateman, K. Blennow, C. C. Rowe, R. A. Sperling, and J. L. Cummings, "Alzheimer's disease," *Nat. Rev. Dis. Prim.*, vol. 1, no. 1, pp. 1–18, 2015.

[14] S. S. Sisodia and R. E. Tanzi, “Alzheimer’s disease: Advances in genetics, molecular and cellular biology,” *Alzheimer’s Dis. Adv. Genet. Mol. Cell. Biol.*, pp. 1–286, 2007, doi: 10.1007/978-0-387-35135-3/COVER.

[15] I. R. Miousse, K. R. Kutanzi, and I. Koturbash, “Effects of ionizing radiation on DNA methylation: from experimental biology to clinical applications,” *Int. J. Radiat. Biol.*, vol. 93, no. 5, pp. 457–469, 2017, doi: 10.1080/09553002.2017.1287454.

[16] J. I. Jacobson, “Electromagnetism in medicine.,” *Indian J. Med. Sci.*, vol. 46, no. 11, pp. 321–327, 1992.

[17] C. Westbrook, “Part 9: Instrumentation,” *MRI a Glance*, pp. 90–96, 2002.

[18] T. M. R. Derneği, *MR Tekniklerine Yönelik MR Fizik Kursu - 2*. Miki Matbaacılık, Ankara: Türkiye.

[19] M. A. Jacobs, T. S. Ibrahim, and R. Ouwerkerk, “AAPM/RSNA physics tutorial for residents - MR imaging: Brief overview and emerging applications,” *Radiographics*, vol. 27, no. 4, pp. 1213–1229, 2007, doi: 10.1148/rg.274065115.

[20] R. A. Pooley, “Fundamental physics of MR imaging,” *Radiographics*, vol. 25, no. 4, pp. 1087–1099, 2005, doi: 10.1148/rg.254055027.

[21] A. Abildgaard, *The Physics of Clinical MR Taught Through Images*, Second., vol. 56, no. 2. Thieme, 2015.

[22] D. McRobbie, w, *MRI From Picture to Proton Cambridge University Press, Second Edition*. Mcrobbie, D.W., Moore, E.A., Graves, M.J., Prince, M.R: Cambridge University Press, 2006.

[23] E. L. W. Giele *et al.*, “Movement correction of the kidney in dynamic MRI scans using FFT phase difference movement detection,” *J. Magn. Reson. Imaging*, vol. 14, no. 6, pp. 741–749, 2001, doi: 10.1002/jmri.10020.

[24] S. Mori and P. C. M. Van Zijl, “A motion correction scheme by twin-echo navigation for diffusion- weighted magnetic resonance imaging with multiple RF echo acquisition,” *Magn. Reson. Med.*, vol. 40, no. 4, pp. 511–516, 1998, doi: 10.1002/mrm.1910400403.

[25] A. Ligeza, *Artificial Intelligence: A Modern Approach*, vol. 9, no. 2. London, 1995.

[26] S. Saini, “Supervised vs. Unsupervised Learning: What’s the Difference?,” *LinkedIn*, 2021. https://www.linkedin.com/pulse/supervised-vs-unsupervised-learning-whats-difference-smriti-saini/ (accessed Jul. 12, 2024).

[27] Y. Huang, “Deep Q-networks,” *Deep Reinf. Learn. Fundam. Res. Appl.*, pp. 135–160, Jan. 2020, doi: 10.1007/978-981-15-4095-0_4.

[28] W. S. Noble, “What is a support vector machine?,” *Nature Biotechnology*, 2006. https://datatron.com/what-is-a-support-vector-machine/ (accessed Jul. 12, 2024).

[29] H. Zhang, “The optimality of Naive Bayes,” *Proc. Seventeenth Int. Florida Artif. Intell. Res. Soc. Conf. FLAIRS 2004*, vol. 2, pp. 562–567, 2004.

[30] N. Verma, “Understanding and Implementing Gaussian Naive Bayes Classification with Python,” *Medium*, 2023. https://medium.com/@nandiniverma78988/understanding-and-implementing-gaussian-naive-bayes-classification-with-python-dbdfcf2939f7 (accessed Jul. 12,

2024).

[31] R. Silipo, “From a single decision tree to a random forest,” *Towards Data Science*, 2019. https://towardsdatascience.com/from-a-single-decision-tree-to-a-random-forest-b9523be65147 (accessed Jul. 12, 2024).

[32] D. M. Atallah, M. Badawy, A. El-Sayed, and M. A. Ghoneim, “Predicting kidney transplantation outcome based on hybrid feature selection and KNN classifier,” *Multimed. Tools Appl.*, vol. 78, no. 14, pp. 20383–20407, Jul. 2019, doi: 10.1007/s11042-019-7370-5.

[33] L. Vinet and A. Zhedanov, *A “missing” family of classical orthogonal polynomials*, vol. 44, no. 8. Springer, 2011.

[34] Y. LeCun, L. Bottou, Y. Bengio, and P. Haffner, “Gradient-based learning applied to document recognition,” *Proc. IEEE*, vol. 86, no. 11, pp. 2278–2323, 1998, doi: 10.1109/5.726791.

[35] Raimi Karim, “Illustrated: 10 CNN Architectures,” *Towards Data Science*, 2019. https://towardsdatascience.com/illustrated-10-cnn-architectures-95d78ace614d#e276 (accessed Jan. 20, 2021).

[36] A. Krizhevsky, I. Sutskever, and G. E. Hinton, “ImageNet classification with deep convolutional neural networks,” *Commun. ACM*, vol. 60, no. 6, pp. 84–90, 2017, doi: 10.1145/3065386.

[37] K. Simonyan and A. Zisserman, “Very deep convolutional networks for large-scale image recognition,” Sep. 2015, [Online]. Available: https://arxiv.org/abs/1409.1556.

[38] C. Szegedy, S. Ioffe, V. Vanhoucke, and A. A. Alemi, “Inception-v4, inception-ResNet and the impact of residual connections on learning,” in *31st AAAI Conference on Artificial Intelligence, AAAI 2017*, 2017, pp. 4278–4284, doi: 10.1609/aaai.v31i1.11231.

[39] F. Chollet, “Xception: Deep learning with depthwise separable convolutions,” in *Proceedings - 30th IEEE Conference on Computer Vision and Pattern Recognition, CVPR 2017*, 2017, vol. 2017-Janua, pp. 1800–1807, doi: 10.1109/CVPR.2017.195.

[40] C. Szegedy *et al.*, “Going deeper with convolutions,” in *Proceedings of the IEEE Computer Society Conference on Computer Vision and Pattern Recognition*, 2015, vol. 07-12-June, pp. 1–9, doi: 10.1109/CVPR.2015.7298594.

[41] K. He, X. Zhang, S. Ren, and J. Sun, “Deep residual learning for image recognition,” in *Proceedings of the IEEE Computer Society Conference on Computer Vision and Pattern Recognition*, 2016, vol. 2016-Decem, pp. 770–778, doi: 10.1109/CVPR.2016.90.

[42] S. Ioffe and C. Szegedy, “Batch normalization: Accelerating deep network training by reducing internal covariate shift,” in *32nd International Conference on Machine Learning, ICML 2015*, 2015, vol. 1, pp. 448–456.

[43] S. Xie, R. Girshick, P. Dollár, Z. Tu, and K. He, “Aggregated residual transformations for deep neural networks,” in *Proceedings - 30th IEEE Conference on Computer Vision and Pattern Recognition, CVPR 2017*, 2017, vol. 2017-Janua, pp. 5987–5995, doi: 10.1109/CVPR.2017.634.

[44] M. B. Karabulut, “Unveiling the Power of ResNet101v2: A Deep Dive into Image Classification,” 2023. https://mtburakk.medium.com/unveiling-the-power-of-resnet101v2-a-deep-dive-into-image-classification-d1a10ad02f29 (accessed Jul. 12, 2024).

[45] D. Galasko, “Expanding the repertoire of biomarkers for Alzheimer’s disease: Targeted and non-targeted approaches,” *Frontiers in Neurology*, vol. 6, no. DEC. p. 256, 2015, doi: 10.3389/fneur.2015.00256.

[46] P. Vemuri *et al.*, “Alzheimer’s disease diagnosis in individual subjects using structural MR images: Validation studies,” *Neuroimage*, vol. 39, no. 3, pp. 1186–1197, 2008, doi: 10.1016/j.neuroimage.2007.09.073.

[47] S. Klöppel *et al.*, “Automatic classification of MR scans in Alzheimer’s disease,” *Brain*, vol. 131, no. 3, pp. 681–689, 2008, doi: 10.1093/brain/awm319.

[48] T. Tong, R. Wolz, Q. Gao, R. Guerrero, J. V. Hajnal, and D. Rueckert, “Multiple instance learning for classification of dementia in brain MRI,” *Med. Image Anal.*, vol. 18, no. 5, pp. 808–818, 2014, doi: 10.1016/j.media.2014.04.006.

[49] K. Ishii *et al.*, “Fully automatic diagnostic system for early- and late-onset mild Alzheimer’s disease using FDG PET and 3D-SSP,” *Eur. J. Nucl. Med. Mol. Imaging*, vol. 33, no. 5, pp. 575–583, 2006, doi: 10.1007/s00259-005-0015-0.

[50] C. Möller *et al.*, “Alzheimer disease and behavioral variant frontotemporal dementia: Automatic classification based on cortical atrophy for single-subject diagnosis,” *Radiology*, vol. 279, no. 3, pp. 838–848, 2016, doi: 10.1148/radiol.2015150220.

[51] H. Il Suk, S. W. Lee, and D. Shen, “Hierarchical feature representation and multimodal fusion with deep learning for AD/MCI diagnosis,” *Neuroimage*, vol. 101, pp. 569–582, 2014, doi: 10.1016/j.neuroimage.2014.06.077.

[52] S. Sarraf and G. Tofighi, “Classification of Alzheimer’s Disease Structural MRI Data by Deep Learning Convolutional Neural Networks,” pp. 8–12, 2016, [Online]. Available: http://arxiv.org/abs/1607.06583.

[53] F. Lozano, A. Ortiz, J. Munilla, A. Peinado, and for the A. s. D. N. Initiative, “Automatic computation of regions of interest by robust principal component analysis. Application to automatic dementia diagnosis,” *Knowledge-Based Syst.*, vol. 123, pp. 229–237, 2017, doi: 10.1016/j.knosys.2017.02.025.

[54] N. Amoroso *et al.*, “Deep learning reveals Alzheimer’s disease onset in MCI subjects: Results from an international challenge,” *J. Neurosci. Methods*, vol. 302, pp. 3–9, 2018, doi: 10.1016/j.jneumeth.2017.12.011.

[55] J. D. Gispert *et al.*, “CSF YKL-40 and pTau181 are related to different cerebral morphometric patterns in early AD,” *Neurobiol. Aging*, vol. 38, pp. 47–55, 2016, doi: 10.1016/j.neurobiolaging.2015.10.022.

[56] N. Pasnoori, T. Flores-Garcia, and B. D. Barkana, “Histogram-based features track Alzheimer’s progression in brain MRI,” *Sci. Rep.*, vol. 14, no. 1, p. 257, 2024, doi: 10.1038/s41598-023-50631-1.

[57] M. Ahmadzadeh *et al.*, “Neuroimaging and machine learning for studying the pathways from mild cognitive impairment to alzheimer’s disease: a systematic review,” *BMC Neurol.*, vol. 23, no. 1, p. 309, 2023, doi: 10.1186/s12883-023-03323-2.

[58] L. Bloch and C. M. Friedrich, “Classification of Alzheimer’s Disease using volumetric features of multiple MRI scans,” *Proc. Annu. Int. Conf. IEEE Eng. Med. Biol. Soc. EMBS*, vol. 2019, pp. 2396–2401, Jul. 2019, doi: 10.1109/EMBC.2019.8857188.

[59] A. Basher, B. C. Kim, K. H. Lee, and H. Y. Jung, “Volumetric Feature-Based Alzheimer’s Disease Diagnosis from sMRI Data Using a Convolutional Neural Network and a Deep Neural Network,” *IEEE Access*, 2021. https://ieeexplore.ieee.org/stamp/stamp.jsp?arnumber=9354805 (accessed Jun. 26, 2024).

[60] N. J. Dhinagar *et al.*, “3D convolutional neural networks for classification of Alzheimer’s and Parkinson’s disease with T1-weighted brain MRI,” p. 62, 2021, doi: 10.1117/12.2606297.

[61] G. Folego, M. Weiler, R. F. Casseb, R. Pires, and A. Rocha, “Alzheimer’s Disease Detection Through Whole-Brain 3D-CNN MRI,” *Front. Bioeng. Biotechnol.*, vol. 8, p. 534592, 2020, doi: 10.3389/fbioe.2020.534592.

[62] B. Khagi and G. R. Kwon, “3D CNN based alzheimer’s diseases classification using segmented grey matter extracted from whole-brain MRI,” *Int. J. Informatics Vis.*, vol. 5, no. 2, pp. 200–205, 2021, doi: 10.30630/joiv.5.2.572.

[63] M. Dyrba *et al.*, “Improving 3D convolutional neural network comprehensibility via interactive visualization of relevance maps: evaluation in Alzheimer’s disease,” *Alzheimer’s Res. Ther.*, vol. 13, no. 1, pp. 1–18, 2021, doi: 10.1186/s13195-021-00924-2.

[64] H. Mzoughi *et al.*, “Deep Multi-Scale 3D Convolutional Neural Network (CNN) for MRI Gliomas Brain Tumor Classification,” *J. Digit. Imaging*, vol. 33, no. 4, pp. 903–915, 2020, doi: 10.1007/s10278-020-00347-9.

[65] R. Basnet, M. O. Ahmad, and M. N. S. Swamy, “A deep dense residual network with reduced parameters for volumetric brain tissue segmentation from MR images,” *Biomed. Signal Process. Control*, vol. 70, no. August, p. 103063, 2021, doi: 10.1016/j.bspc.2021.103063.

[66] C. R. Jack *et al.*, “The Alzheimer’s Disease Neuroimaging Initiative (ADNI): MRI methods,” *J. Magn. Reson. Imaging*, vol. 27, no. 4, pp. 685–691, Apr. 2008, doi: 10.1002/jmri.21049.

[67] C. Gaser, “CAT A Computational Anatomy Toolbox for SPM - Voxel-based morphometry (VBM),” 2010. https://neuro-jena.github.io/cat/index.html#VBM (accessed Oct. 12, 2019).

[68] G. Flandin and K. Friston, “Statistical parametric mapping (SPM),” *Scholarpedia*, 2008. https://www.fil.ion.ucl.ac.uk/spm/ (accessed Oct. 10, 2019).

[69] C. Rorden, L. Bonilha, J. Fridriksson, B. Bender, and H. O. Karnath, “Age-specific CT and MRI templates for spatial normalization,” *Neuroimage*, vol. 61, no. 4, pp. 957–965, 2012, doi: 10.1016/j.neuroimage.2012.03.020.

[70] L. W. Johnson and E. R. Girden, “ANOVA: Repeated Measures,” *J. Mark. Res.*, vol. 32, no. 2, p. 243, 1995, doi: 10.2307/3152054.

[71] F. Shi, *Learn About Wilks’ Lambda in SPSS With Data From the Global Health Observatory (2016)*. SAGE Publications, Ltd., 2019.

[72] D. Cramer and D. Howitt, “Mauchly’s test of sphericity,” *The SAGE Dictionary of Statistics*, 2015. https://www.ibm.com/support/knowledgecenter/en/SSLVMB_23.0.0/spss/tutorials/glmr_testmarket_mauchly.html (accessed Mar. 01, 2020).

[73] W. Vogt, “Levene’s Test,” in *Dictionary of Statistics & Methodology*, 2015.

[74] W. Vogt, “Tukey’s Honestly Significant Difference (HSD) Test,” in *Dictionary of Statistics & Methodology*, 2015.

[75] M. Hall, E. Frank, G. Holmes, B. Pfahringer, P. Reutemann, and I. H. Witten, “The WEKA data mining software,” *ACM SIGKDD Explor. Newsl.*, vol. 11, no. 1, pp. 10–18, 2009, doi: 10.1145/1656274.1656278.

[76] R. Parikh, A. Mathai, S. Parikh, G. C. Sekhar, and R. Thomas, “Understanding and using sensitivity, specificity and predictive values,” *Indian J. Ophthalmol.*, vol. 56, no. 1, pp. 45–50, 2008, doi: 10.4103/0301-4738.37595.

[77] M. Ahmadzadeh, T. D. Cosco, J. R. Best, G. J. Christie, and S. DiPaola, “Predictors of the rate of cognitive decline in older adults using machine learning,” *PLoS One*, vol. 18, no. 3 March, p. e0280029, Mar. 2023, doi: 10.1371/journal.pone.0280029.

[78] Y. Lecun, Y. Bengio, and G. Hinton, “Deep learning,” *Nature*, vol. 521, no. 7553. pp. 436–444, 2015, doi: 10.1038/nature14539.

[79] C. R. Jack *et al.*, “Hypothetical model of dynamic biomarkers of the Alzheimer’s pathological cascade,” *Lancet Neurol.*, vol. 9, no. 1, pp. 119–128, 2010, doi: 10.1016/S1474-4422(09)70299-6.

[80] B. C. Dickerson and D. A. Wolk, “MRI cortical thickness biomarker predicts AD-like CSF and cognitive decline in normal adults,” *Neurology*, vol. 78, no. 2, pp. 84–90, 2012, doi: 10.1212/WNL.0b013e31823efc6c.

[81] S. Liu, S. Liu, W. Cai, S. Pujol, R. Kikinis, and D. Feng, “Early diagnosis of Alzheimer’s disease with deep learning,” in *2014 IEEE 11th International Symposium on Biomedical Imaging, ISBI 2014*, 2014, pp. 1015–1018, doi: 10.1109/isbi.2014.6868045.

[82] G. Ciaburro and B. Venkateswaran, *Neural network with R: Smart models using CNN, RNN, deep learning, and artificial intelligence principles*, vol. 91. Packt Publishing Ltd, 2017.

[83] Muhammad Fouzan, “Understanding LSTM, GRU, and RNN Architectures,” *Medium*, 2023. https://medium.com/@mfouzan144/understanding-lstm-gru-and-rnn-architectures-e0b3a0c1d741 (accessed Jul. 12, 2024).

[84] W. Zaremba, I. Sutskever, and O. Vinyals, “Recurrent Neural Network Regularization,” 2014.

[85] Y. Yu, X. Si, C. Hu, and J. Zhang, “A review of recurrent neural networks: Lstm cells and network architectures,” *Neural Comput.*, vol. 31, no. 7, pp. 1235–1270, Jul. 2019, doi: 10.1162/neco_a_01199.

[86] H. Choi and K. H. Jin, “Predicting cognitive decline with deep learning of brain metabolism and amyloid imaging,” *Behav. Brain Res.*, vol. 344, pp. 103–109, 2018, doi: 10.1016/j.bbr.2018.02.017.

[87] M. Bakator and D. Radosav, “Deep learning and medical diagnosis: A review of literature,” *Multimodal Technol. Interact.*, vol. 2, no. 3, 2018, doi:

10.3390/mti2030047.

[88] A. Gupta, M. S. Ayhan, and A. S. Maida, “Natural image bases to represent neuroimaging data,” *30th Int. Conf. Mach. Learn. ICML 2013*, no. PART 3, pp. 2024–2031, 2013, Accessed: Oct. 17, 2023. [Online]. Available: www.fil.ion.ucl.ac.uk/spm/.

[89] P. M. Müller and C. Meisel, “Spatial and temporal correlations in human cortex are inherently linked and predicted by functional hierarchy, vigilance state as well as antiepileptic drug load,” *PLoS Comput. Biol.*, vol. 19, no. 3, 2023, doi: 10.1371/journal.pcbi.1010919.

[90] J. Deng, W. Dong, R. Socher, L.-J. Li, Kai Li, and Li Fei-Fei, “ImageNet: A large-scale hierarchical image database,” pp. 248–255, Mar. 2010, doi: 10.1109/cvpr.2009.5206848.

[91] Princeton University, “About WordNet. WordNet.,” *Princeton University.*, 2010. http://wordnet.princeton.edu (accessed Jun. 28, 2021).

[92] X. Long, L. Chen, C. Jiang, and L. Zhang, “Prediction and classification of Alzheimer disease based on quantification of MRI deformation,” *PLoS One*, vol. 12, no. 3, 2017, doi: 10.1371/journal.pone.0173372.

[93] J. You and J. Korhonen, “Deep Neural Networks for No-Reference Video Quality Assessment,” *Proc. - Int. Conf. Image Process. ICIP*, vol. 2019-Septe, pp. 2349–2353, Sep. 2019, doi: 10.1109/ICIP.2019.8803395.

[94] S. Montaha, S. Azam, A. K. M. R. H. Rafid, M. Z. Hasan, A. Karim, and A. Islam, “TimeDistributed-CNN-LSTM: A Hybrid Approach Combining CNN and LSTM to Classify Brain Tumor on 3D MRI Scans Performing Ablation Study,” *IEEE Access*, vol. 10, pp. 60039–60059, 2022, doi: 10.1109/ACCESS.2022.3179577.

[95] A. Ebrahimi, S. Luo, and for the A. Disease Neuroimaging Initiative, “Convolutional neural networks for Alzheimer’s disease detection on MRI images,” *J. Med. Imaging*, vol. 8, no. 02, 2021, doi: 10.1117/1.jmi.8.2.024503.

[96] L. Hang, “Keras: Time CNN+LSTM for video recognition,” 2019. https://stackoverflow.com/questions/54696029/keras-time-cnnlstm-for-video-recognition (accessed Jul. 12, 2024).

CURRICULUM VITAE

Education & Professional Experiences:

2007 – 2013	B.Sc., Electrical and Electronics Engineering, TOBB Economics and Technology University, Ankara, TURKEY
2014 – 2017	M.Sc., Biomedical Engineering, Erciyes University, Kayseri, TURKEY
2017 – 2024	Ph.D., Electrical and Computer Engineering, Abdullah Gul University, Kayseri, TURKEY
2019 – 2020	Research Intern, Biotechnology Engineering, Ben-Gurion University of the Negev, Be'er-Sheva, ISRAEL
2020 – Present	Lecturer, Medical Imaging Techniques, Halil Bayraktar Vocational Health College, Erciyes University, Kayseri

Fellowships/Awards:

2019 – 2020	Research Fellow at Academic Internship Program, Negev Ben-Gurion University, Beer Sheva, Israel
2017 – 2020	100/2000 YOK (Turkish Council of High Education) fellowship for Doctorate
2015 – 2016	Fellowship for project of "Development of 3D MRI acquisition based on non-cartesian k-space trajectories" from The Scientific and Technological Research Council of Turkey (Tubitak)
2015	First Rank Best Poster Presentation in International Biomedical Engineering Congress 2015, Nicosia, North Cyprus

Publications:

Dündar, M. S., Gümüş, K., & Yılmaz, B. (2024). MR Görüntülemede K-Uzayının Kartezyen Olmayan Yörüngelerle 3 Boyutlu Örneklenmesi. *Gazi Üniversitesi Mühendislik Mimarlık Fakültesi Dergisi*, 8.

Dundar, M. S., Belanová, I., Bonetti, G., Gelanová, V., & Kozáčiková, R. (2024). Genetic variants in genes correlated to the PI3K/AKT pathway: the role of ARAP3, CDH5, KIF11, and RELN in primary lymphedema. *Lymphology*, 19.

Ismail A. B., Dundar M. S., Erguzeloglu C. O., Ergoren M. C., Alemdar A., Ozemri Sag S. & Temel, S. G. (2024). Alzheimer disease associated loci: APOE single nucleotide polymorphisms in Marmara region. *Biomedicines*, vol.12, no.5, 968. doi:10.3390/biomedicines12050968

Dundar, M. S., Yildirim, A., Yildirim, D. T., Akalin, H., & Dündar, M., (2024). Artificial cells: A potentially groundbreaking field of research and therapy. *Eurobiotech Journal*, vol.8, no.1, 55-64. doi:10.2478/ebtj-2024-0006

Senturk, N., Tuncel, G., Dogan, B., Aliyeva, L., Dundar, M. S., Ozemri Sag, S., Mocan, G., Temel, S. G., Dundar, M., & Ergoren, M. C. (2021). BRCA variations risk assessment in breast cancers using different artificial intelligence models. *Genes*, 12(11), 1774. https://doi.org/10.3390/genes12111774

Acer, N., Baysal, H., Dündar, M. S., Gültekin, M., & Dönmez, H., (2019). Brain volume differences in Huntington disease using MRI. *Erciyes Medical Journal*, vol.41, no.1, 4-5.

Acer, N., Dündar, M. S., & Bastepe-Gray, S., (2018). What does the water inside the brain tell us? Diffusion tensor imaging. *Eurobiotech Journal*, vol.2, 177-179. doi:10.2478/ebtj-2018-0047

Kacmaz, R. N., Yılmaz, B., Dündar, M. S., & Dogan, S., (2018). Motion artifact detection in colonoscopy images. *Eurobiotech Journal*, vol.2, 171-175. doi:10.2478/ebtj-2018-0022

Ciraci, S., Gumus, K. Z., Doğanay, S., Dündar, M. S., Ozcora, G. D. K., Görkem, S. B., ... Per, H. (2017). Diagnosis of intracranial calcification and hemorrhage in pediatric patients: Comparison of quantitative susceptibility mapping and phase images of susceptibility-weighted imaging. *Diagnostic And Interventional Imaging*, vol.98, 707-714. doi:10.1016/j.diii.2017.05.004

Presentations:

Oral Presentation of "Automatic Classification of Alzheimer's Disease Based on MRI Volumetric Features", European Biotechnology Congress, Valencia/Spain, April 2019

Oral Presentation of "Automatic Blurry Colon Image Detection Using Laplacian Operator Based Features", European Biotechnology Congress, Athens/Greece, April 2018

Poster Presentation of “Shell Trajectory Sampling Of K-Space in Magnetic Resonance Imaging”, European Biotechnology Congress, Riga/Latvia, May 2016

Poster Presentation of “Computerized Intracranial Tumor Detection Using Morphological Operations On MRI”, European Biotechnology Congress, Riga/Latvia, May 2016

Oral Presentation of “QSM and SWI Phase Imaging in Diagnosis of Intracranial Calcification and Hemorrhage in Pediatric Cases”, TMRD 2016, Ankara/Turkey, May 2016

Oral Presentation of “Identification of Intracranial Calcifications and Hemorrhages Using MRI-Based Quantitative Susceptibility Mapping”, European Biotechnology Congress, Bucharest/Romania, May 2015

Poster Presentation of “Quantitative Susceptibility Mapping in Identification of Intracranial Hemorrhage: A Case Report”, International Biomedical Engineering Congress, Nicosia/North Cyprus, March 2015